REMOTE CONTROL OF CELL FUNCTION USING TEMPERATURE AS AN INPUT

WILLIAM BENMAN

A DISSERTATION

in

BIOENGINEERING

Presented to the Faculties of the University of Pennsylvania

in

Partial Fulfillment of the Requirements for the

Degree of Doctor of Philosophy

2024

Supervisor of Dissertation

Lukasz J. Bugaj

Assistant Professor of Bioengineering

Graduate Group Chairperson

Daniel A. Hammer

Alfred G. and Meta A. Ennis Professor

Dissertation Committee

Danial A. Hammer, Alfred G. and Meta A. Ennis Professor

Matthew Good, Associate Professor of Cell and Developmental Biology

Mark Sellmyer, Assistant Professor of Radiology

To Sharvari, who makes everything in my life possible

ACKNOWLEDGMENT

The following individuals have contributed to this work either directly or by providing guidance: William Benman[1], Zikang Huang[1], Ayush Pal[1], Pavan Iyengar[2], Liang Dong[1], David Gonzalez-Martinez[1], Thomas Mumford[1], Erin Berlew[1], Delaney Wilde[1], Hao Deng[3], Caitlyn Parker[4], Ivan A. Kuznetsov[1], Bomyi Lim[3,6], Arndt F. Siekmann[4,6], Brian Chow[1], Lukasz J. Bugaj[1,5,6]

Affiliations:

[1]Department of Bioengineering, University of Pennsylvania, Philadelphia, PA, 19104, USA

[2]Department of Biophysics, University of Pennsylvania, Philadelphia, PA, 19104, USA

[3]Department of Chemical and Biomolecular Engineering, University of Pennsylvania, Philadelphia, PA, USA

[4]Department of Cell and Developmental Biology and Cardiovascular Institute, Perelman School of Medicine at the University of Pennsylvania, Philadelphia, PA, USA

[5]Abramson Cancer Center, University of Pennsylvania, Philadelphia, PA, 19104, USA

[6]Institute of Regenerative Medicine, University of Pennsylvania, Philadelphia, PA, 19104, USA

We thank C. Seiler and the CHOP Aquatic Zebrafish Core for assistance in injecting and mounting zebrafish embryos, D. Wu and D. Chenoweth for assistance with TIRF microscopy and H. Johnson and J. Toettcher (Princeton) for providing Drosophila S2 cells. The authors thank Dr. James Shorter (Penn) and Dr. Steven Boeynaems (Baylor) for helpful discussions. This work was supported by the National Science Foundation (CAREER CBET 2145699 to L.J.B., GRFP to W.B., CAREER MCB1652003 for E.E.B. and B.Y.C.), the National Institutes of Health (R35GM138211, R21GM132831 to L.J.B, R35GM133425 for H.D. and B.L., R01NS101106 for E.E.B and B.Y.C. and R01HL152086 to A.F.S.), and the Penn Center for

Precision Engineering for Health (CPE4H). Cell sorting was performed on a BD FACSAria Fusion that was obtained through an NIH S10 grant (S10OD026986).

ABSTRACT

REMOTE CONTROL OF CELL FUNCTION TEMPERATURE AS AN INPUT

William Benman

Lukasz Bugaj

The increasing prevalence of RNA and cell-based therapies such as CAR-T, encapsulated cells, and gene therapies have generated a need to control cell function deep inside the body. However, traditional methods of deep-tissue cell actuation require injection of chemicals which can suffer from poor uptake, clearing, and a lack of spatio/temporal precision. Newer methods such as optogenetics suffer from the inability of light to penetrate tissue beyond a few millimeters. An attractive solution to overcome this challenge is using temperature as an inducer. Temperature can be regulated at distances of 10s of centimeters using safe and clinically approved technology such as focused ultrasound or hot/cold compresses. In this work, we develop a modular protein actuator that responds to small changes in temperature. We used this system to thermally control a wide variety of cellular functions including proteolysis, nuclear shuttling, Ras/Erk signaling, cell size, and cell death. Finally, we demonstrate that these tools can be used to non-invasively, locally activate cell death in cancer xenografts in mice.

TABLE OF CONTENTS

LIST OF FIGURES

INTRODUCTION

Emerging cell therapies require precision control

The advent of cell, gene, and RNA therapies has led to promising new therapeutic options for diseases ranging from muscular dystrophy to cancer. CAR-T therapies, whereby T-cells are engineered to target specific cancer markers, have proven highly effective in the treatment of certain leukemias and lymphomas[1]. CRISPR-based gene therapies offer exciting potential for correcting genetic diseases[2]. Recent advances in the delivery of RNA to target cells in-vivo could lead to a new class of “smart” drugs by expressing proteins that can sense and respond to complex environmental states within the cells[3,4].

However, with the growing complexity of these therapies comes more complex side effects. Hyperactivation of CAR-T cells can lead to widespread toxicity throughout the body[5]. Genetic modification in organs outside the target organ can lead to long term complications including cancer[6]. These severe side effects demonstrate the critical necessity for exogenous, clinician-controlled regulation of these cutting-edge therapies. The ability to regulate the function of cell/genetic therapies would greatly enhance the safety and efficacy of such treatments, limiting their activation to only target loci within the body and allowing tuning of their activity based on monitoring of the patient.

Current control methods are limited in tissue

Recent advances have enabled rapid, modular design of systems to convert exogenous signals into a desired cellular response. These systems often consist of a protein that when exposed to a particular input, undergoes a conformational change that alters its function. Of particular utility are protein modules that undergo stereotyped and consistent changes in response to an input such as chemicals or light. When fused to a particular effector, these protein modules can translate the input into a change in cellular function[7]. For example, the

widely used FKBP/FRB protein pair undergoes dimerization in the presence of the small molecule, rapamycin. Fusing FKBP to a DNA binding domain and FRB to a transcription activation domain allows rapamyacin to mediate the binding of the DNA binding domain to the transcription activation domain to control gene expression[8]. Recent work has described a chemically inducible clustering system used to control effectors activated by clustering[9]. Optogenetics has perhaps seen the greatest proliferation of these protein tools, with several undergoing processes ranging from dimerization[10–14], allostery[15,16], oligomerization[17], ion transport[17,18], and membrane recruitment [19,20] when exposed to different wavelengths of light.

While these tools offer the ability to control cell function in artificial cell cultures, they are significantly more difficult to implement in vivo. Chemical inputs are difficult to regulate in both space and time as different molecules exhibit differential rates of diffusion, clearance, and cannot be easily removed post-administration. Meanwhile, light suffers from poor penetration in tissue, with visible wavelengths rapidly attenuating with every millimeter of tissue depth. Therefore, there are few methods for precise, spatio-temporally defined control of biochemistry deep in patient tissue.

Temperature is a promising in-vivo inducer

Temperature has gained recent interest as a dynamic and penetrant inducer[21–24]. Unlike light, temperature can be readily controlled in tissues. Simple application of an ice pack or heat pad can change tissue temperature. For deeper and more precise control, focused ultrasound can be used to heat tissue with sub-millimeter-scale spatial resolution[25]. Furthermore, unlike either chemical- or light-induction, thermal-responsiveness could uniquely interface with an organism's own stimuli, setting the stage for engineered biological systems that autonomously detect and respond to physiological temperature cues, for example fevers or inflammation.

Development of a novel thermogenetic tool

The widespread adoption of chemo– and opto-genetic proteins was enabled by the identification of protein domains that undergo stereotyped and consistent changes in response to small molecules or light. However, remarkably few analogous temperature-sensing modules have been described, limiting their widespread implementation.

In recent work by Glantz et. al. a novel photoreceptor, BcLOV4, was described and characterized. BcLOV4 reversibly binds the cell membrane when exposed to blue light. We initially used this capability to build new tools for optical control of cell signaling including the Ras/Erk and PI3K signaling pathways. However, while developing these tools, we discovered that in addition to light, BcLOV membrane binding can be mediated by temperature. We characterized this temperature dependence in wild type BcLOV and determined its effect on BcLOV light sensitivity. Furthermore, we explored the potential of BcLOV to serve as a purely thermogenetic actuator, enabling control of cell behavior in response to small changes in temperature. This BcLOV based tool, which we named Melt, enabled localized activation of cell death in subcutaneous cancer populations in mice, demonstrating the utility of thermogenetics for in-vivo precision control of biochemistry.

CHAPTER 1: BCLOV-BASED OPTOGENETIC SIGNALING PROBES DEMONSTRATE SENSITIVITY TO TEMPERATURE

Portions of this chapter was previously published/is in press as:

Benman, W., Berlew, E.E., Deng, H. et al. *"Temperature-responsive optogenetic probes of cell signaling."* Nat Chem Biol 18, 152–160 (2022). https://doi.org/10.1038/s41589-021-00917-0

W.B. was the primary author of this manuscript.

Background

The goal of this work was to utilize BcLOV4 to create optogenetic probes of cell signaling. Optogenetic probes permit light-induced control of intracellular biochemistry. Such probes are typically engineered from proteins that evolved to respond to their host's environmental conditions, i.e. to its light status[36,37]. Light-responsive actuators now exist for control of protein dimerization[10–14], allostery[15,16], oligomerization[17], ion transport[17,18], and membrane recruitment [19,20] providing an extensive toolset for precise manipulation of an array of biological processes, including cell signaling.

Ras and phosphatidyl inositol-3-kinase (PI3K) are signaling regulators that together control essential cell processes including transcription, translation, growth, survival, proliferation and migration[38–41]. Optogenetic control of these two pathways has enabled recent discoveries of how their spatiotemporal dynamics regulate cell and tissue growth, form, and disease[42–45]. Currently, optogenetic activation of Ras or PI3K is achieved through membrane recruitment of signaling effectors via light-induced protein heterodimerization[46,47]. However, this approach is limited by the necessity for two distinct proteins, which can require stoichiometric tuning of both components to permit signaling through a large dynamic range with minimal elevated basal signaling[48]. While stoichiometric tuning is feasible in single cells, it is more challenging in tissues and organisms.

Single-component membrane translocation was recently described using the BcLOV4 photoreceptor, which translocates from the cytoplasm to membrane phospholipids under blue light in mammalian cells[19] (**Figure 1A**). BcLOV4 has already served as a modular technology for light-induced activation of the Rho GTPases Rac1[49], RhoA[49,50], Cdc42[51], suggesting that BcLOV4 may be adapted to regulate many additional pathways. In this work, our initial goal was to generate and characterize BcLOV4-based probes for Ras or PI3K activation.

Generation of BcLOV based signaling probes

To generate an actuator of Ras/Erk signaling, we fused BcLOV4 to the catalytic domain of the Ras guanine nucleotide exchange factor Son of Sevenless 2 (SOScat), which activates Ras upon recruitment to the membrane (**Figure 1B**)[47]. We generated an analogous probe to control PI3K signaling by replacing the SOScat domain with the inter-SH2 domain of the p85 subunit (iSH) (**Figure 1C**)[46,52]. We refer to these probes as BcLOV-SOScat and BcLOV-iSH, respectively.

To test probe activity, we illuminated NIH 3T3 cells that stably expressed either BcLOV-SOScat or BcLOV-iSH, and we quantified levels of phospho-Erk (ppErk) or phosho-Akt (pAkt) using immunofluorescence imaging. In the absence of blue light, BcLOV-SOScat cells exhibited low basal levels of ppErk, similar to wild-type (wt) cells. Upon illumination, ppErk levels rose dramatically and reached their peak within 5 minutes, reaching levels comparable to wt cells stimulated with 10% serum (**Figure 1D**). BcLOV-iSH expressing cells also induced strong levels of pAkt, although basal activation in the absence of light was somewhat higher relative to wt cells (**Figure 1E**). These results suggest that our BcLOV-derived probes stimulate physiologically relevant levels of pathway activation while minimally disrupting endogenous cell physiology in the dark state.

To better characterize light-induced stimulation of BcLOV-SOScat and BcLOV-iSH, we measured the dose-response of signal activation as a function of light intensity. We found that

BcLOV-SOScat achieves half-maximal pathway stimulation with 7 mW/cm2 of blue light and saturates near 40 mW/cm2 with a 4-fold signal induction (**Figure 1F**). Conversely, we estimate that BcLOV-iSH reaches half-maximal signal induction with 80 mW/cm2, though we did not reach saturation at the highest levels of stimulation (4-fold at 160 mW/cm2) (**Figure 1G**). Taken together, given the large fold-change induction, minimal basal level of stimulation, and single-component nature, BcLOV4-based probes offer several beneficial qualities for optogenetic stimulation of Ras and PI3K signaling.

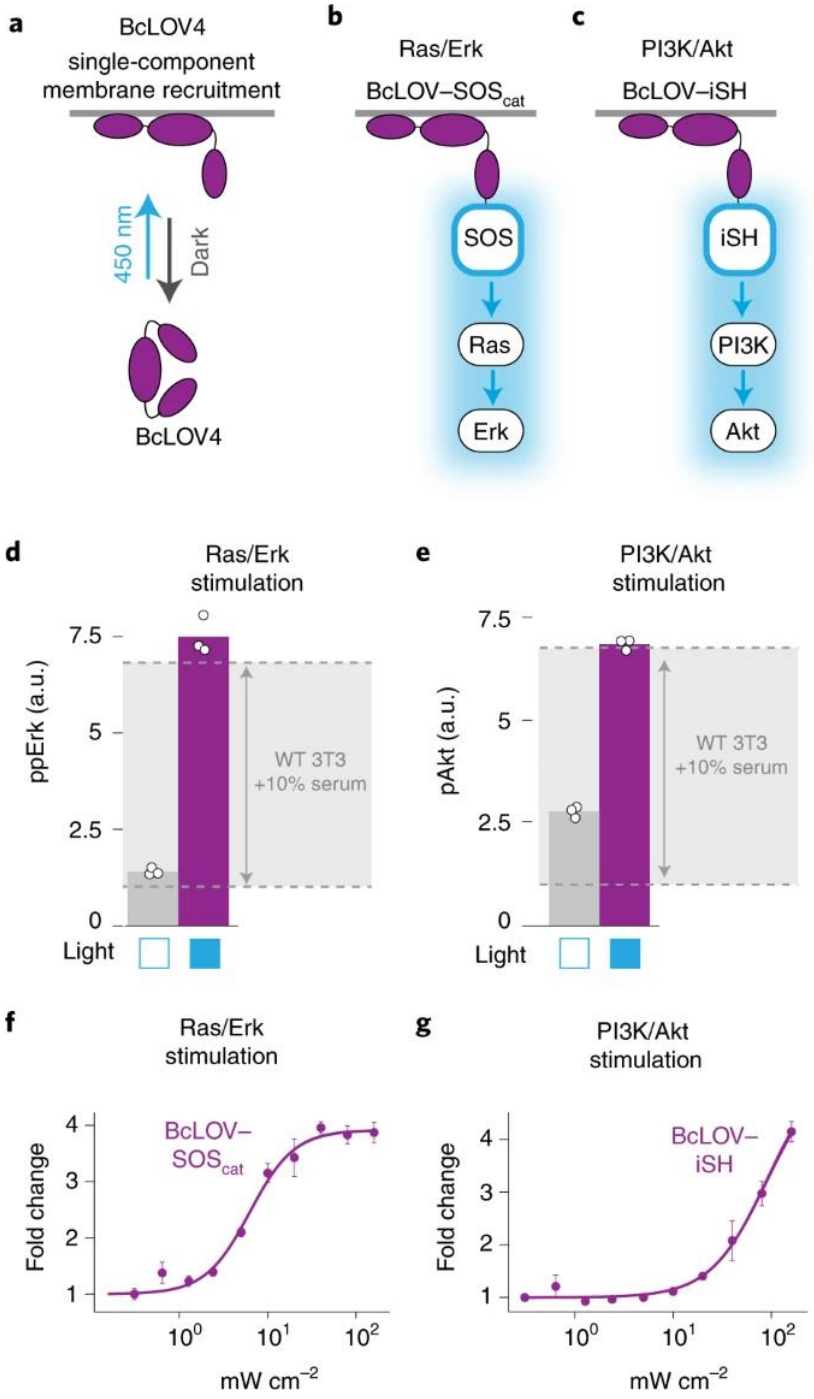

Figure 1: Single-component BcLOV4 fusions allow control of Ras and PI3K signaling

A) BcLOV4 binds the cell membrane when exposed to blue light. The three BcLOV4 domains represent the LOV, DUF and RGS domains, as previously described[19]. B) Light-induced membrane recruitment of BcLOV4 fused to the SOScat catalytic domain will induce Ras/Erk

signaling. C) Analogous recruitment of the iSH domain will induce PI3K/Akt signaling. D,E) Five minutes of blue-light stimulation (160 mW cm−2 at 20% duty cycle) increases intracellular ppErk levels in cells that express BcLOV–SOScat (D) and increases pAkt in cells that express BcLOV–iSH (E). a.u., arbitrary units. Gray zone indicates the change in ppErk or pAkt in wild-type cells that were stimulated with 10% calf serum for 10 min. Data represent means of three biologically independent replicates, each representing the mean signal intensity from approximately 2,000 to 4,000 single cells. F,G) Light intensity dose-response of (F) ppErk fold-change induction in BcLOV–SOScat-expressing cells or (G) pAkt fold-change induction in BcLOV–iSH cells at 100% duty cycle after 5 min of illumination. Data represent means ± s.d. of three biologically independent replicates, each representing the mean signal intensity from approximately 300 to 500 single cells. All stimulation in A–G was achieved using the optoPlate-96.

BcLOV signaling probes demonstrate temperature sensitivity

After successfully generating BcLOV4-based signaling probes, we next asked how these probes could regulate signaling through time. We used recently-described illumination devices for microwell plates (the optoPlate-96) to perform time course stimulation experiments[48]. After stimulation, cells were immunostained and quantified to assess pathway activity (**Figure 2A**).

We were surprised to find that, despite constant stimulation for 60 minutes, cells that expressed BcLOV-SOScat showed an initial increase followed by rapid and complete decay of ppErk (**Figure 2B**). To determine if transient signaling was caused by BcLOV4 or alternative mechanisms (e.g. negative feedback within the Ras/Erk pathway), we compared activation dynamics to those achieved with an orthogonal optogenetic system, the commonly-used blue-light inducible iLID/sspB (nano) heterodimerizing pair, which can be adapted to recruit SOScat to the membrane (iLID-SOScat[44]). In contrast to BcLOV-SOScat, iLID-SOScat produced stable

signaling under identical illumination conditions, indicating that Ras/Erk signal decay was a feature of BcLOV4 stimulation. Similarly, sustained illumination of BcLOV-iSH cells led to an initial increase followed by rapid decrease of pathway activity, whereas stimulation with an analogous iLID-based probe (iLID-iSH) resulted in sustained activity. These results further indicate that transient activation dynamics were a function of BcLOV4 activation and not the pathway under study.

To understand the nature of signal decay, we performed a series of experiments using the BcLOV-SOScat probe. We first asked whether BcLOV-SOScat inactivation could be reversed after removal of the light stimulus. We stimulated cells with blue light until the signal decayed, withdrew light for either 0.5, 1, or 3 hr, and then restimulated for 10 minutes (**Figure 2C**). As before, the initial 45 minutes of blue light led to a pulse of ppErk signal. However, only ~10% of the original signal could be obtained upon restimulation even after 3 hrs of light withdrawal. These results suggest that BcLOV4 can undergo a spontaneous transition into an uncharacterized, long-lived inactivated state.

We next asked whether certain experimental parameters could modulate the observed signal decay rate. We noticed that pathway decay kinetics could change as a function of the illumination settings of individual experiments. Because higher light intensity can also cause heating of the sample[48], we tested the effects of both temperature and light on BcLOV-SOScat stimulation kinetics. To perform optogenetic time course experiments at specific temperatures, we adapted the optoPlate-96 to precisely control both illumination as well as sample temperature (**Figure 2D,E**). Briefly, we decoupled sample heating from the illumination profile by designating 24 LED positions for light stimulation and using the remaining 72 LED positions as heating elements (**Figure 2D**). Illumination of the 72 “heater” LEDs over 3000 intensity levels correlated linearly with sample temperature in the wells above the 24 “stimulation” LEDs (R2 = 0.99) (**Figure 2E**).

Strikingly, we observed that BcLOV-SOScat decay kinetics were strongly correlated to sample temperature, where signal decay was faster at higher temperatures (**Figure 2F,G**). At the extremes, ppErk decayed with a half-life of ~6 minutes at 42 °C, while decay was minimal at 30 °C. We observed strong ppErk signal induction at all temperatures tested, suggesting that temperature only impacted BcLOV4 function in its lit, activated form. By contrast, iLID-SOS-induced signaling was sustained at both high and low temperatures (**Figure 2G**), further indicating that temperature sensitivity is a property of BcLOV4 control.

We also observed that BcLOV-SOScat signal decay rate was dependent on light intensity, where higher intensity led to rapid decay, while lower intensity led to more sustained stimulation (**Figure 2H**). Low light achieved sustained signaling at the expense of signal amplitude, although we note that this tradeoff will be specific to the pathway under study. For example, in a previous report, comparable sparse illumination conditions (1.6% duty cycle) yielded saturating activation levels of BcLOV-regulated Rho GTPase signaling[48–50].

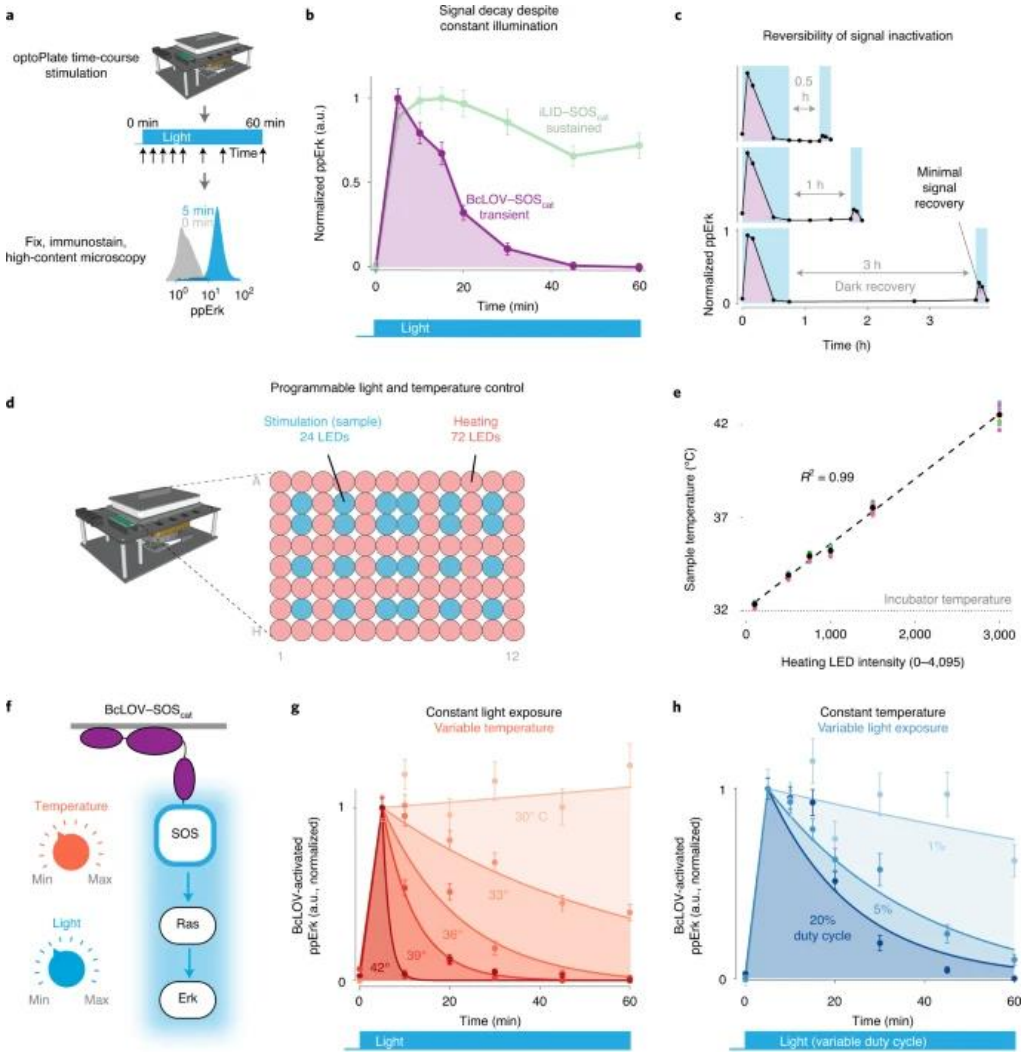

Figure 2: BcLOV-induced signaling dynamics depend on temperature and light exposure. A) Schematic of experimental protocol. B) Sustained stimulation of BcLOV–SOScat (160 mW cm−2 at 20% duty cycle) reveals that the ppErk signal decays rapidly after an initial increase, whereas activation by iLID–SOScat remains sustained. C) Recovery (dark) periods of up to 3 h after signal decay do not permit recovery of activatable BcLOV–SOScat, suggesting that BcLOV4 inactivation is effectively irreversible. D) BcLOV–SOScat signal dynamics were examined under variable light and temperature conditions. E) Schematic for how the optoPlate-96 was repurposed to allow independent control of experimental light and temperature conditions. F) Steady-state sample temperature was a linear function of the intensity of the 72

heater LEDs (precise intensity–temperature relationship should be determined empirically for each individual optoPlate). G) At a given light exposure level (here, 160 mW cm−2 at 20% duty cycle), BcLOV–SOScat signal decays more rapidly at higher temperatures. H) At a given temperature (here, 36 °C), BcLOV–SOScat decay increases with increased light exposure (variable duty cycles of 160 mW cm−2 light). Data points in (B), (C), (G) and (H) represent the mean ± s.e.m. of ~1,000–4,000 individual cells. Traces in (G) and (H) are exponential decay functions fit to data points at each temperature and duty cycle, as described in the Methods section. Data are normalized between the minimum and maximum of each trace. Normalization was performed separately for each temperature and duty cycle to highlight the change in the rate of BcLOV–SOScat inactivation rather than absolute signal.

Characterization of BcLOV temperature sensitivity

Because signal decay was observed with both the BcLOV-SOScat and BcLOV-iSH probes but not with analogous iLID-based probes (**Figure 2B**), we suspected that the observed light- and temperature-dependent decay kinetics were a property of the BcLOV4 photosensor itself. We thus quantified membrane translocation of BcLOV-mCherry under various light and temperature conditions (**Figure 3A**). In accordance with our signaling results, sustained illumination resulted in sustained membrane localization at low temperatures (25 °C) but only transient localization at 37 °C, with inactivated BcLOV4 returning to the cytoplasm after ~30 min (**Figures 3 B,C**). Similarly, when we varied light intensity at a constant temperature, increased intensity (duty cycle) increased the decay rate of membrane translocation (**Figure 3D**). Together, these data demonstrate that BcLOV4 acts as not only a photosensor but also a temperature sensor.

To explain and predict BcLOV-mCh translocation dynamics, we developed a computational model. We reasoned that, in addition to the dark and lit states, a third state of

BcLOV4 could account for our observations of light- and temperature-dependent decay kinetics (**Figure 3E**). This third state, which we call the temperature-inactivated (TI) state, is only accessible from the lit (membrane-bound) state, and transition to the TI state is irreversible on the timescales we consider (**Figure 2C**). We predicted that the rate of entry into the TI state (k3) would increase as a function of temperature. Thus, because more light increases the amount of BcLOV4 in the lit state, and higher temperature increases the transition rate from the lit to the TI state, our model could explain why both increased light and temperature can increase the decay rate of BcLOV4 membrane translocation. For details on model development, see Figure 3E-G. We parameterized our model by fitting values for k1, k2, and k3 to live-cell data of BcLOV-mCh translocation dynamics over a range of temperatures (25-40 °C) and light exposures (1.1%, 3.3%, 10% duty cycle) (**Figure 3E,F**). Across experimental conditions, we obtained consistent values for k1 and k2, which correspond closely to reported values of BcLOV4 membrane translocation and dissociation (half-times of ~1 second for association and ~1 minute for dissociation)[19]. As expected, k3 showed a strong exponential dependence on temperature. We then used our parameterized model to generate a 2D heatmap of predicted BcLOV4 decay rate as a function of temperature and light dose during sustained stimulation (**Figure 3G**). This heatmap represents a systematic roadmap of translocation dynamics that can be used to predict the behavior of BcLOV4-based probes.

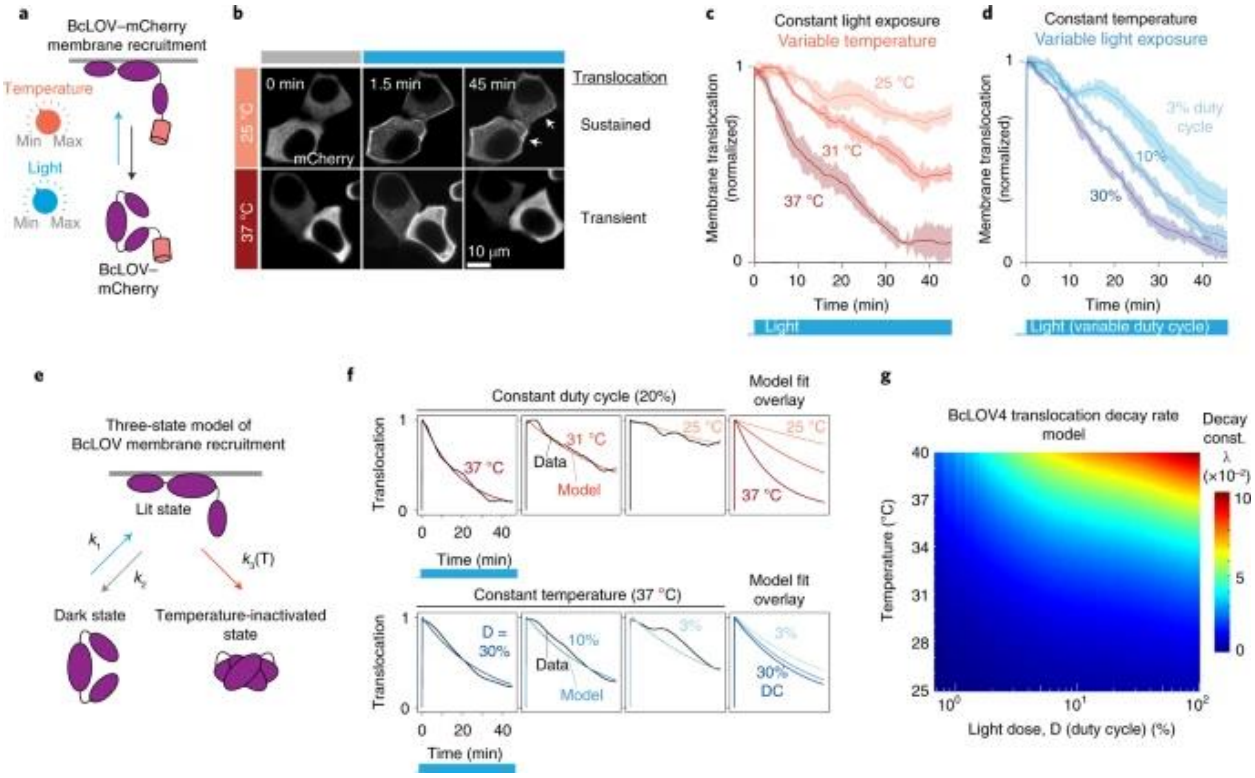

Figure 3: BcLOV4 membrane translocation dynamics depend on temperature and light exposure.

A) BcLOV–mCherry membrane recruitment was quantified at various temperatures and light exposures using live-cell imaging. B) Representative images of membrane recruitment at low and high temperatures. Activation at 25 °C permitted sustained membrane recruitment, whereas recruitment at 37 °C was transient (stimulation performed at 1.45 W cm−2 and 3% duty cycle). Image brightness was adjusted at each time point for clarity to account for photobleaching. C) Quantification of membrane recruitment at various temperatures (1.45 W cm−2 at 3% duty cycle) reveals a temperature-dependent decay of membrane translocation. D) Quantification of membrane recruitment at various light exposures (at 36 °C and 1.45 W cm−2) shows light-dependent decay of BcLOV–mCherry translocation. Each trace is the mean membrane fluorescence ± s.e.m. of three biologically independent samples, with each replicate

representing the mean of ~100 cells. E) Schematic of a three-state model of BcLOV4 membrane translocation. F) Fitting the model to live-cell translocation data provides parameter values for k1, k2 and k3 (T). G) Heatmap depicts the decay rate of BcLOV4 membrane localization as a function of temperature and light exposure. Decay rates were calculated by simulating sustained illumination over a range of duty cycles and temperatures and fitting the modeled decay rate to a single exponential decay. Color indicates the decay constant **λ** (1 divided by the time to reach 37% of maximum signal). Larger **λ** indicates faster decay.
BcLOV temperature sensitivity can predict behavior of BcLOV based signaling probes

Modeling Predicts Behavior of BcLOV-based Signaling Probes

To validate our model and predict signaling dynamics downstream of BcLOV-SOScat stimulation, we integrated our model of membrane translocation with a model of Ras/Erk signal transmission (**Figure 4A**). We modeled the Ras/Erk pathway with a transfer function that represents signal transmission from membrane-localized SOScat to Erk phosphorylation as a dynamic filter. Previous work defined the Ras/Erk module as a second-order low pass filter (LPF) with a 2 mHz cutoff frequency[47]. However, this previous work applied SOScat membrane localization as an input and measured nuclear localization of fluorescently-tagged Erk2 as the output, whereas in our case the output was cytoplasmic levels of endogenous ppErk. Thus, to choose the most appropriate model, we performed dynamic stimulation of BcLOV-SOScat and fitted either first- or second-order low-pass filter models to the data. We found that signal transmission was best modeled by a first-order LPF with a cutoff frequency of 2 mHz (**Figure 4B,C**). Because first order filters transmit fast signal dynamics more efficiently than analogous second-order filters (**Figure 4B**), our results suggest that the Ras/Erk pathway can transmit fast signal fluctuations (< ~4 min) more effectively than previously measured. Our results may differ from previous measurements because of additional biochemical steps required to transduce

phosphorylation into nuclear translocation of fluorescently-tagged Erk, compared to the direct observation of Erk phosphorylation in our work. Notably, our model captured both the fast timescale dynamics of ppErk fluctuations, as well as the slow timescale decay of ppErk due to progressive BcLOV4 inactivation (**Figure 4C**).

Our integrated model of membrane translocation and Erk activation predicted how specific light and temperature inputs shape BcLOV-SOScat-induced ppErk dynamics. We used this model to generate a heatmap of ppErk decay rate as a function of temperature and light dose during constant illumination (**Figure 4D**). To validate our model, we performed stimulation time course experiments at temperature and light conditions that were sampled from regions of our heatmap with diverse decay rates. Measured ppErk decay rates matched closely to the rates predicted by our model over all experimental conditions tested (**Figure 4D**). Together, our data and models comprehensively describe how BcLOV4 and optogenetic probes thereof will behave as a function of light and temperature condition. We note, however, that decay rates will likely vary between pathways due to pathway-specific biochemisty and must thus be determined empirically.

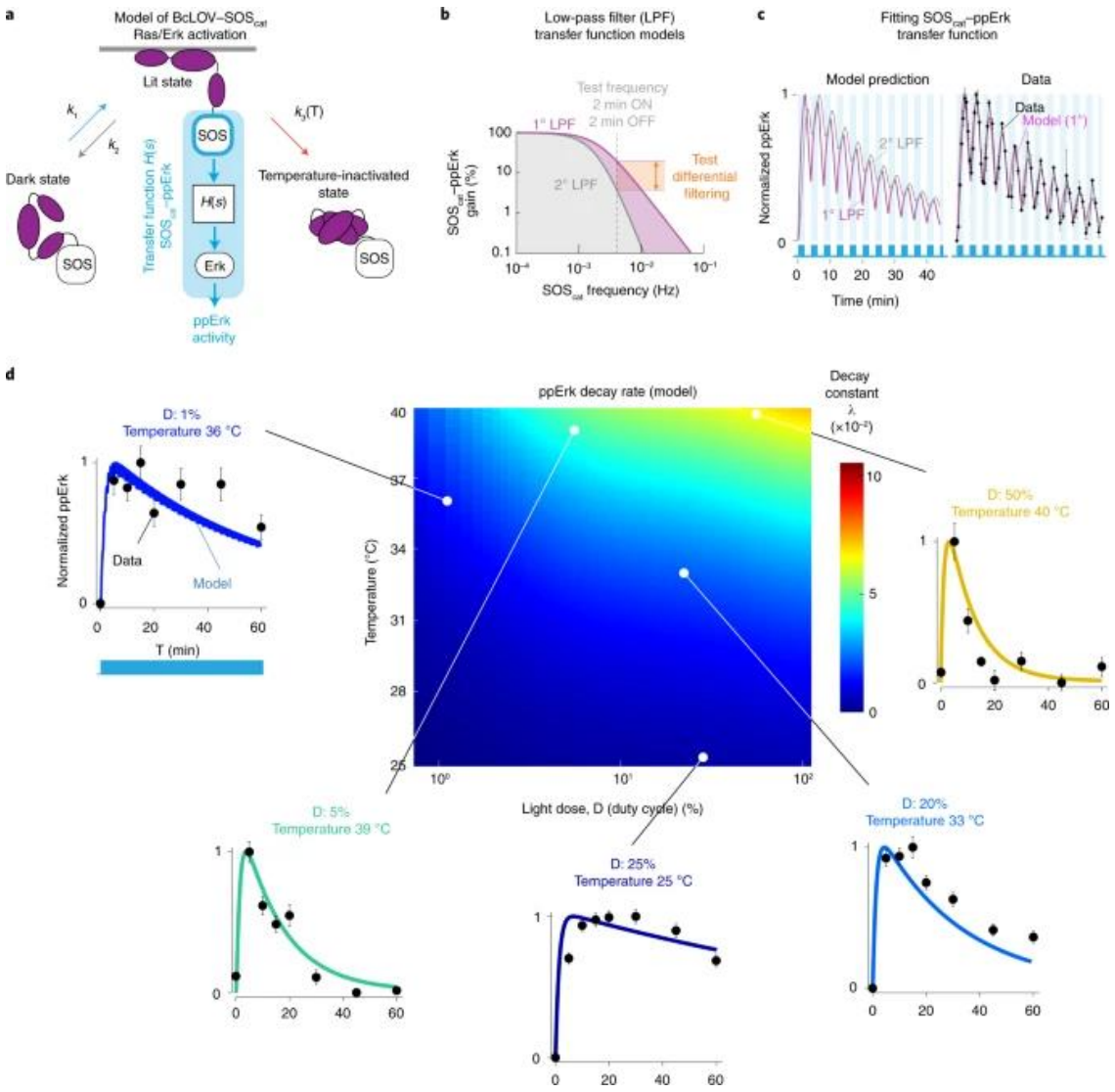

Figure 4: Modeling predicts BcLOV–SOScat-induced ppErk dynamics and reveals dynamic

A) A model of ppErk activation was developed by integrating the BcLOV4 membrane translocation model with a transfer function model that describes the input/output response of SOScat membrane localization (input) to ppErk activation (output). B) Filtering properties of a 1° versus 2° LPF. 1° LPFs attenuate high-frequency inputs less than 2° LPFs. C) A 1° LPF with 2-mHz cutoff frequency best describes ppErk dynamics when stimulated with fast 2 min ON/2 min

OFF BcLOV–SOScat oscillations. Data points are the mean ± s.d. of three biologically independent replicates, with each replicate representing the mean of ~1,000–2,000 cells. D) Heatmap depicts the predicted Erk activation dynamics resulting from BcLOV4 membrane translocation dynamics over the indicated light and temperature conditions. Plots show model predictions of Erk activation at the indicated experimental conditions, and data points show experimental results. Data points represent means ± s.e.m. of ~1,000–4,000 cells. See Methods for model details.

BcLOV based signaling probes are suitable for use in low temperature organisms

The single-component nature and low rate of spontaneous decay at < 30 °C position BcLOV4-based tools as highly suited for experiments in tissues and model organisms that operate at lower temperatures. We thus tested performance of BcLOV4 and BcLOV-SOScat in both zebrafish embryos and Drosophila S2 cells. BcLOV-mCh expressed well in zebrafish embryos and, upon illumination, rapidly translocated to the membrane in all cells (**Figure 5A**). Membrane translocation was sustained through 90 min of illumination, as expected from our experiments in mammalian cells (**Figure 5B**). To determine whether BcLOV-SOScat could stimulate Ras signaling in zebrafish, we co-expressed BcLOV-SOScat with the ErkKTR reporter, which has previously been used in zebrafish (**Figure 5C**)[53]. In cells that co-expressed BcLOV-SOScat and ErkKTR-BFP, we observed rapid and reversible ErkKTR translocation that could be stimulated over multiple cycles (**Figure 5D**), consistent with our data from mammalian cells. Notably, over 90 min of sustained stimulation, Erk activity remained high, demonstrating that both BcLOV-SOScat translocation and signal activation could be maintained (**Figure 5E**). We also expressed BcLOV4 probes in Drosophila S2 cells as an orthogonal model system that grows at temperatures permissive to stable BcLOV4 translocation, and we again observed sustained BcLOV-mCh membrane localization through 90 min of blue light illumination (**Figure**

5F,G). Furthermore, expression and sustained stimulation of BcLOV-SOScat allowed sustained activation of ppErk (**Figure 5H**). Together, these data show that BcLOV4-based probes can serve as simple and sensitive optogenetic probes across diverse cells, tissues, and organisms of study.

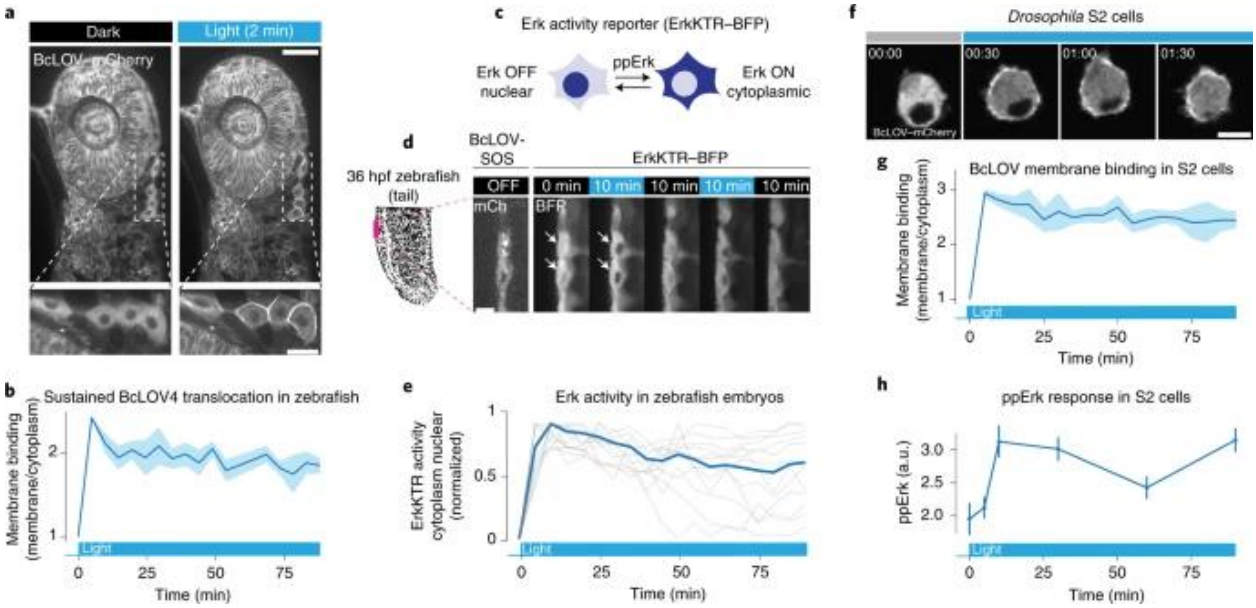

Figure 5: BcLOV4 and BcLOV–SOScat in zebrafish embryos and Drosophila cells.

A) Blue-light-induced membrane translocation of BcLOV–mCherry in a zebrafish embryo (24 h post fertilization (hpf)). Scale bar, 50 μm; inset scale bar, 20 μm. B) BcLOV–mCherry translocation is sustained over 90 min in zebrafish embryos. Data represent mean ± s.d. of ten cells. C) Schematic of ErkKTR activity. ErkKTR is nuclear when Erk signaling is off and translocates to the cytoplasm when Erk is activated. D) The Ras/Erk pathway can be reversibly stimulated over multiple cycles in zebrafish embryos (24 hpf) that coexpress BcLOV–SOScat and ErkKTR–BFP, as measured by ErkKTR–BFP translocation. White arrows highlight nuclei where ErkKTR translocation is evident. Scale bar, 10 μm. E) Sustained illumination of BcLOV–SOScat permits sustained elevated Erk activity in 24 hpf zebrafish embryos. Plot shows ErkKTR cytoplasmic/nuclear ratios of 12 single cells (light gray; blue trace represents mean) measured

over two experiments. Trajectories are normalized between 0 and 1 to permit comparison between experiments. For (A)–(E) stimulation was performed using 1.45 W cm−2 488 nm light at 1.5% duty cycle. F) BcLOV–mCherry membrane translocation in Drosophila S2 cells stimulated with blue light (1.45 W cm−2 at 3% duty cycle) for 90 min. Scale bar, 10 μm. G) Quantification of (f) shows sustained membrane translocation in S2 cells. Data represent mean ± s.d. of ten cells. H) Sustained stimulation of BcLOV–SOScat in S2 cells shows sustained elevated ppErk levels over 90 min, measured by immunofluorescence. Data represent the mean ± s.d. of three biologically independent samples, with each replicate representing the mean of ~100–200 cells.. Stimulation was performed at (160 mW cm−2 at 20% duty cycle). All experiments shown in Fig. 5 were performed at room temperature. a.u., arbitrary units.

Discussion

We describe the application of BcLOV4 membrane translocation to generate single-component probes for optical control over Ras/Erk or PI3K signaling. We characterized these probes in mammalian cells and found that the BcLOV4-based probes can provide signaling through a large, physiologically relevant dynamic range with low basal signaling and high photosensitivity. In addition, BcLOV4-based probes are single-protein systems, eliminating the need for stoichiometric tuning of analogous multicomponent tools. Such tuning can be difficult in model organisms like Drosophila and zebrafish, in which we show that BcLOV4-based probes function well. More generally, our work adds to the growing library of BcLOV4-based optogenetic signaling tools[49–51], highlighting BcLOV4 as a modular optogenetic actuator of effector/membrane interaction to regulate signaling across biological models, including yeast, flies, zebrafish and mammalian cells[19,49].

We discovered that BcLOV4 is a temperature sensor in addition to its known role as a photosensor. Although temperature-dependence has been observed in certain photosensors

and optogenetic probes, this dependence mostly manifests as decreased protein stability or photoreactivity at elevated temperatures[14,54–58]. By contrast, BcLOV4 folds and translocates rapidly when exposed to light at all temperatures, but then, under sustained illumination, enters a long-lived inactive state and reverts to the cytoplasm at a rate that increases with both temperature and light dose (Figs. 2, 3). This behavior is consistent with a temperature-dependent photoinactivation in which, once BcLOV4 is at the membrane in its active state, elevated temperatures accelerate its transition into a state that is incompatible with membrane binding.

We developed quantitative models of BcLOV4 membrane translocation and signal activation to predict activity as a function of light and temperature. We found that sustained, whole-cell illumination will result in sustained translocation only under low light exposure or low temperature. These conditions may explain why BcLOV4 inactivation was not previously noticed, as its use to date has been performed at either <30 °C or over short periods, necessitated only sparse illumination (~1% duty cycle), or used subcellular regions of stimulation, which preserves unstimulated, activatable BcLOV4 outside the region of illumination[19,49,50].

Combined with previous work, our studies provide a roadmap for how to use BcLOV4-based optogenetic tools. BcLOV4 membrane recruitment can be faithfully and precisely controlled over short durations (less than ~30 min) across temperatures but requires low temperatures or sparse illumination for sustained (>30 min) stimulation. Specific BcLOV4 translocation dynamics over a range of light and temperature conditions can be predicted using our three-state model (Fig. 3e–g). Most importantly, our work suggests that BcLOV function can be regulated by temperature, suggesting potential for BcLOV to serve as a solely thermogenetic actuator, independent of light. Based on this work, we chose to focus our efforts on engineering a version of BcLOV that could be actuated solely by temperature.

CHAPTER 2: ENGINEERING A MODULAR THERMOGENETIC ACTUATOR

Portions of this chapter was previously published/is in press as:

William Benman et. al. *"A temperature-inducible protein module for control of mammalian cell fate."* bioRxiv 2024.02.19.581019; doi: https://doi.org/10.1101/2024.02.19.581019

W.B. was the primary author of this manuscript.

Background

The goal of this work was to generate a modular, single component thermogenetic protein module. Inducible proteins permit on-demand, remote control of cell behavior, for example using chemicals or light as inputs. These inputs trigger protein conformational changes that can regulate a vast array of downstream protein and cell behaviors in a modular manner. While chemical control requires delivery of a small molecule, light can be applied remotely and offers further benefits for precision in both space and time, as well as low cost of the inducer. There is tremendous potential to extend these benefits into more complex settings including in 3D cell and tissue models, in patients for control of cell therapy, or in dense bioreactors for bioproduction. However, optical control is limited in these more opaque settings because visible light cannot penetrate, for example scattering within millimeters of entering human tissue[59,60]. There is thus a need for alternative inducer strategies that couple the penetration of chemical induction with the spatiotemporal precision of optogenetics.

Temperature has gained recent interest as a dynamic and penetrant inducer[21–24]. Unlike light, temperature can be readily controlled in tissues. Simple application of an ice pack or heat pad can change tissue temperature. For deeper and more precise control, focused ultrasound can be used to heat tissue with sub-millimeter-scale spatial resolution[25]. Furthermore, unlike either chemical- or light-induction, thermal-responsiveness could uniquely interface with an

organism's own stimuli, setting the stage for engineered biological systems that autonomously detect and respond to physiological temperature cues, for example fevers or inflammation.

The widespread adoption of chemo– and opto-genetic proteins was enabled by the identification protein domains that undergo stereotyped and consistent changes in response to small molecules or light. However, remarkably few analogous temperature-sensing modules have been described. Endogenous heat shock promoters have been used for thermal control of transcription, including to induce tumor clearance by engineered cells[22,26,27]. However heat shock promoters can respond to non-thermal stimuli[28–30], and thermal response profiles cannot be readily tuned because they depend on the cell's repertoire of heat shock factor proteins. Moreover, many desirable cell behaviors (e.g. migration, proliferation, survival/death) cannot be easily controlled at the transcriptional level. At the post-translational level, temperature-sensitive (Ts) mutants are protein variants that denature at elevated temperatures[31–33]. However, Ts mutations are generally not modular or reversible and must be laboriously validated for each individual target. The TlpA protein from Salmonella forms thermolabile dimers[34] and underlies existing thermosensitive engineered proteins, including a temperature-controlled dimerization module[35]. However TlpA-based dimers are large (~600-700 amino acids in combined size), and may be limited by the need for stoichiometric tuning between the two components. The identification of distinct temperature-responsive proteins, especially with functions beyond dimerization, is critical for broad development and application of thermogenetic approaches.

Here we introduce a unique thermoresponsive protein module called Melt (Membrane localization using temperature), which we derived from the naturally light- and temperature-sensitive BcLOV4 protein[61]. Melt is a single protein that clusters and binds the plasma membrane at low temperatures but dissociates and declusters upon heating. Using live-cell imaging coupled with custom devices for precise temperature control in 96-well plates[23], we found that Melt could be toggled between these two states rapidly and reversibly, with

observable membrane dissociation and recovery within 10s of minutes. The Melt approach was highly modular, allowing thermal control of diverse processes including EGFR and Ras signaling, TEVp proteolysis, subcellular localization, cytoskeletal rearrangements, and cell death, all through simple end-to-end fusion of the appropriate effectors. We then tuned Melt to increase its switch point temperature above the native 30°C. Such tuning resulted in Melt variants that operated with switch point temperatures between 30-40°C, including ones that bound the membrane at 37°C and fully dissociated at 39°C or 41°C, temperature ranges suitable for downstream application in mammalian tissues. Finally, Melt controlled localized cell death within human cancer xenografts in mice. Thus Melt offers a straightforward, tunable, and broadly applicable platform for endowing thermal control of proteins, cells, and organisms.

Developing a thermoresponsive protein

BcLOV4 is a modular optogenetic protein that natively responds to both blue light and temperature[19,61] (**Figure 6A**). Light stimulation triggers its clustering and translocation from the cytoplasm to the plasma membrane, where it binds anionic phospholipids[19,62]. However, its persistence at the membrane requires both continued light and a permissive temperature. At temperatures above 29°C, membrane binding is transient; BcLOV4 binds but then returns to the cytoplasm (**Figure 6A-C**) at a rate that increases with temperature. Our previous report found that, once dissociated due to elevated temperatures, BcLOV4 remains in the cytoplasm and no longer responds to light stimuli[61]. However, we found that lowering temperature below the 29°C threshold reversed this inactivation and restored light-dependent membrane localization (**Figure 6C**). Thus, temperature alone could be used to toggle the localization of BcLOV4 given the continued presence of blue light.

We sought to harness this thermal responsiveness to generate a protein actuator that responded only to temperature. We reasoned that a BcLOV4 variant with a point mutation that

mimicked the “lit” state would localize to the membrane independent of light status but should retain thermal sensitivity (**Figure 6D**). We thus introduced a Q355N mutation that disrupts the dark-state interaction between the Jα helix and the core of the LOV domain[19,63], generating a variant that was insensitive to light stimulation (**Figure 6D-G**). In HEK 293T cells at 37°C, BcLOV(Q355N)-mCh was expressed in the cytoplasm. Strikingly, shifting the temperature from 37°C to 25°C triggered an accumulation of the protein at the plasma membrane, where increasing accumulation was observed within minutes and continued over the next three hours (**Figure 6D-H**). In contrast to BcLOV(Q355N), the wt photosensitive BcLOV4 did not accumulate at the membrane in response to temperature in the absence of light (**Figure 6G,H**). Thus, BcLOV4(Q355N)—henceforth referred to as Melt (Membrane Localization using Temperature)—represents a protein whose subcellular localization can be regulated solely by temperature.

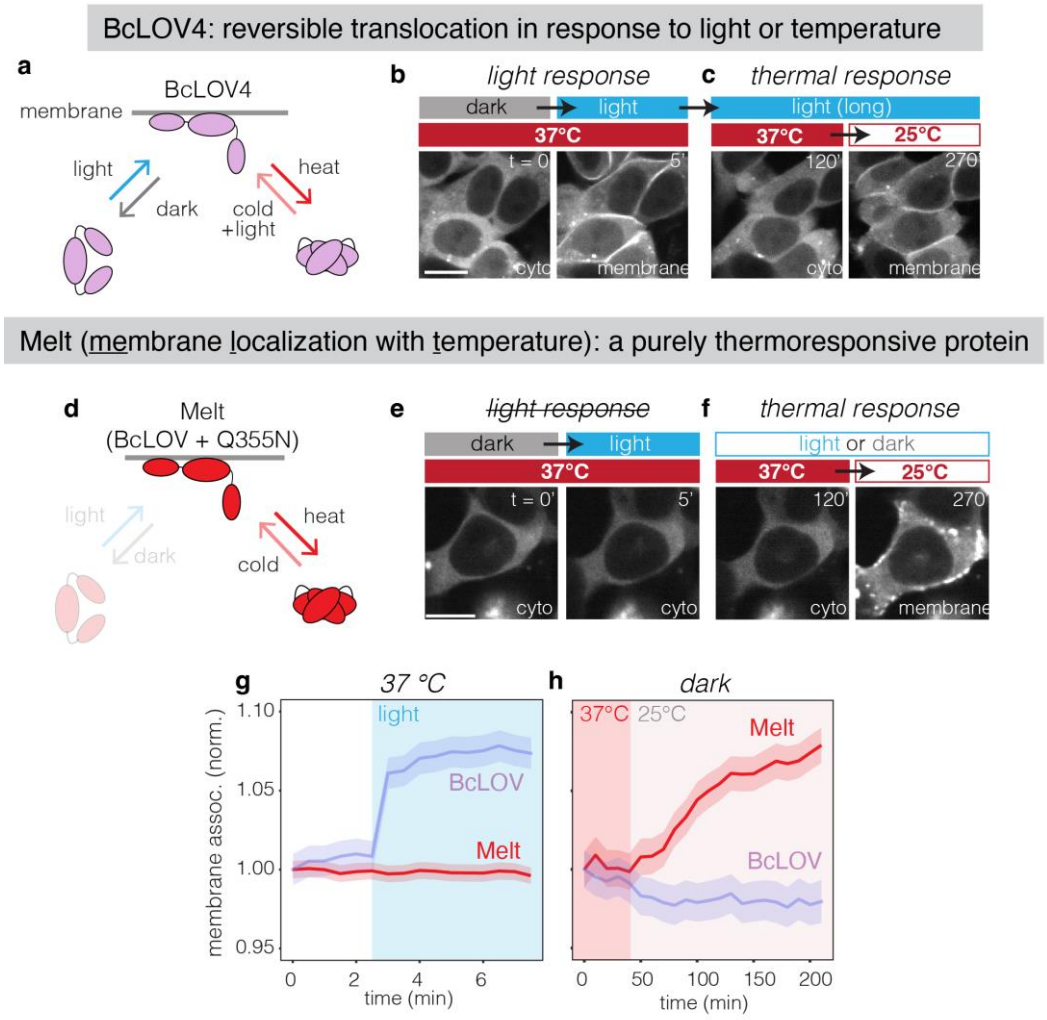

Figure 6: Harnessing BcLOV4 thermosensitivity to generate a purely temperature-inducible protein.

A) Schematic of BcLOV4, a naturally light- and temperature-responsive protein. BcLOV4 translocates to the membrane under blue light and reverts to the cytoplasm in the dark. From the membrane-bound (lit) state, elevated temperatures induce dissociation from the membrane, and lower temperatures induce reassociation. B) Representative images showing translocation to the membrane when exposed to blue light in HEK 293T cells. Scale bar = 15 µm. C) Extended illumination at elevated temperatures (2 hr at 37°C, left) causes subsequent

disassociation from the membrane, but reversion to lower temperatures (right) allows reassociation with the membrane. D) Schematic of Melt (BcLOV4(Q355N)), which mimics the lit state of BcLOV4. E) Representative images showing that Melt is cytoplasmic at 37°C and does not respond to light (E). However, Melt retains temperature sensitivity and translocates to the membrane upon lowering temperature (F). Scale bar = 15 µm. Comparison of optical (G) and thermal (H) responses of wt BcLOV and Melt. Data represent mean +/- 1 SEM of ~100 cells. Each construct was normalized to its first timepoint.

Characterizing Melt performance

We characterized the thermal response properties of Melt, including how the amplitude and kinetics of membrane dissociation/reassociation varied with time and temperature. To systematically explore this large parameter space, we used the thermoPlate, a device for rapid, programmable heating of 96-well plates[23]. Importantly, the thermoPlate can maintain distinct temperatures in multiple wells simultaneously while also permitting live-cell imaging of the sample using an inverted microscope (**Figure 7A,B**).

We first measured steady-state membrane association over a range of temperatures after 14 hrs of heating (**Figure 7C**). Membrane association was maximal at 27°C and minimal at 32°C, and reached 50% of this range at ~30°C, which we assign as its switch temperature. At temperatures above 32°C, Melt membrane association was undetectable and indistinguishable from that of a soluble mCherry. Next, we tested the capacity for dynamic control of Melt. Pulsatile control of temperature between 27°C and 37°C during live cell imaging showed reversible membrane binding and dissociation over multiple cycles **Figure 7G,H**).

We next examined the kinetics of Melt translocation to and from the membrane. Dissociation kinetics increased with higher temperatures (**Figure 7F**). Notably, although steady-

state membrane association was unchanged above 32°C (**Figure 7C**), the rate with which Melt reached this steady state level continued to increase with temperature (note the higher decay rate at 34°C and 37°C relative to 32°C, (**Figure 7F**)). Reassociation kinetics depended on the history of thermal stimulation. Samples that were stimulated at higher temperatures showed a lower degree of reversibility (**Figure 7G**). Reversibility was also a function of the duration of prior stimulation. Although dissociation after 30 min of heating at 37°C was fully reversible, longer stimulation led to smaller degrees of reversion (**Figure 7H**). Collectively, these data suggest that Melt is a thermoswitch that operates tunably and reversibly within a 27-32°C range, but whose reversibility is a function of the magnitude of its prior stimulation.

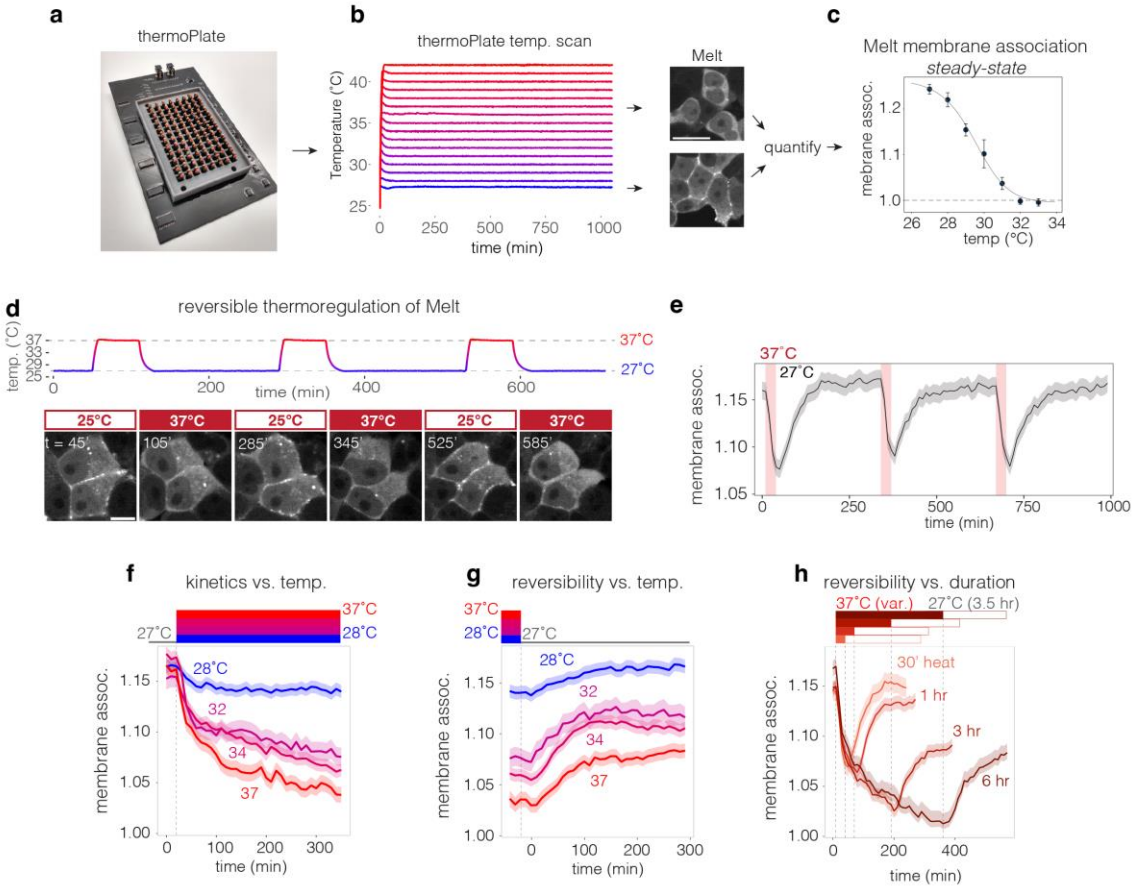

Figure 7: Characterization of Melt membrane association.

A) The thermoPlate is a device for thermal control of individual wells in 96-well plate format. B) Heating of 16 individual wells in a 96-well plate with <1°C resolution over 16 hours. Each trace represents the temperature in a single well as recorded by the thermoPlate. Representative images show HEK 293T stably expressing Melt maintained at either 37°C or 28°C via the thermoPlate for 14hr. Scale = 20 µm. C) thermoPlate heating of HEK 293T cells stably expressing Melt allowed measurement of steady-state membrane association (14 hr of heating). Data points represent mean +/- 1 SD of ~200 cells from each of 3 wells. Dashed line represents membrane association levels of a soluble mCherry. D) Representative images of live-cell images showing Melt membrane binding over multiple cycles of 1 hr at 37°C followed by 3 hr at 27°C. Scale bar = 10 µm. E) Plot of membrane bound Melt while undergoing cycles of 30 min at 37°C followed by 5 hr at 27°C. Traces represent mean +/- 1 SEM of ~100 cells. F) Kinetics of Melt membrane dissociation when exposed to various temperatures after 24 hr of culture at 27°C. G) Kinetics of Melt membrane reassociation at 27°C after prior exposure to 6 hrs of the indicated temperatures. H) Kinetics of Melt membrane reassociation at 27°C after prior exposure to 37°C for the indicated durations. Each trace in (F-H) represents the mean +/- 1 SEM of ~1000 cells. Data were collected from HEK 293T cells that stably expressed Melt-mCh.

Melt permits temperature sensitive control of diverse biochemistry

We explored the potential of Melt to control molecular circuits in mammalian cells in response to temperature changes. Recruitment of cargo to/from the membrane is a powerful mode of post-translational control, including for cell signaling[64]. We first targeted signaling through the Ras-Erk pathway, a central regulator of cell growth and cancer. We generated an end-to-end fusion of Melt to the catalytic domain of the Ras activator SOS2[47], an architecture that previously allowed potent stimulation of Ras signaling using optogenetic BcLOV4[61]. We expressed this construct (MeltSOS) in HEK 293T cells and measured Erk activation upon

changing temperature from 37°C to 27°C (**Fig 8A**). Active Erk (phospho-Erk, or ppErk) could be observed even within 5 minutes of temperature change to 27°C and continued to rise until its plateau at 30 mins (**Fig 8B,C**). Conversely, shifting temperature from 27°C back to 37°C resulted in measurable signal decrease within 5 min and full decay within 30 mins (**Figure 8B,C**), comparable to the kinetics of thermal inactivation during optogenetic stimulation of BcLOV-SOS[61].

Separately, we tested whether we could leverage the clustering of Melt for control of signaling from the receptor level. We generated a fusion of Melt to the intracellular domain of the epidermal growth factor receptor (EGFR) (**Figure 8D**). EGFR is a receptor tyrosine kinase with important roles in development and tumorigenesis and stimulates intracellular signaling through multiple pathways, including Ras-Erk[65]. Importantly, both membrane recruitment and clustering of the EGFR intracellular domain are required for its activation[62,66]. In cells expressing MeltEGFR, lowering the temperature from 37°C to 27°C activated strong Erk signaling within 10 minutes, and reversion to 37°C caused signal decay within 5 minutes, with full decay within 30-60 mins (**Figure 8E,F**). Thus, the inducible membrane recruitment and clustering of Melt can be used for rapid, potent, and reversible thermal control of signaling in a modular fashion.

When Melt activates proteins at the membrane, it operates as a heat-OFF system. We next examined whether Melt could also implement a heat-ON system by coupling membrane translocation to negative regulation. Proteases can negatively regulate their targets through protein cleavage in both natural and synthetic systems[67–69]. We thus tested whether Melt could regulate proteolysis at the membrane. We fused Melt to the viral TEV protease (MeltTEVp) and we measured whether its membrane recruitment could trigger a membrane-associated reporter of TEVp activity, FlipGFP [36] (FlipGFP-CAAX). FlipGFP is non-fluorescent until proteolytic cleavage allows proper folding and maturation of the chromophore (**Figure 8G**). Cells that expressed MeltTEVp and FlipGFP-CAAX showed minimal levels of fluorescence when cultured

at 37°C, similar to cells that expressed FlipGFP-CAAX and cytoplasmic TEVp. However, culturing MeltTEVp cells at lower temperatures for 24 hours increased FlipGFP fluorescence, with fluorescence increasing monotonically with decreasing temperature, whereas cells expressing cytoplasmic TEVp remained at baseline fluorescence (**Figure 8H,I**). Thus, Melt can implement thermal control of proteolysis.

A second way to convert Melt to heat-ON is to regulate its subcellular compartmentalization. Here, the plasma membrane would sequester Melt, and heat would release sequestration and allow translocation to a separate compartment where it could perform a desired function. As a proof of concept, we engineered Melt to regulate nuclear localization by fusing it to sequences that facilitate nuclear import and export (**Figure 8J**).. Melt fused to the SV40 NLS[70] and the Stradα NES[71] showed strong membrane binding and nuclear exclusion at 27°C and nuclear enrichment when heated to 37°C (**Figure 8K,L**). This construct could be dynamically shuttled to and from the nucleus through repeated rounds of heating and cooling. By contrast, Melt without NLS/NES showed no nuclear accumulation upon heating (**Figure 8K,L**). Collectively, our results show that Melt can be applied to control a variety of molecular events, in either heat-ON or heat-OFF configuration, in a straightforward and modular manner.

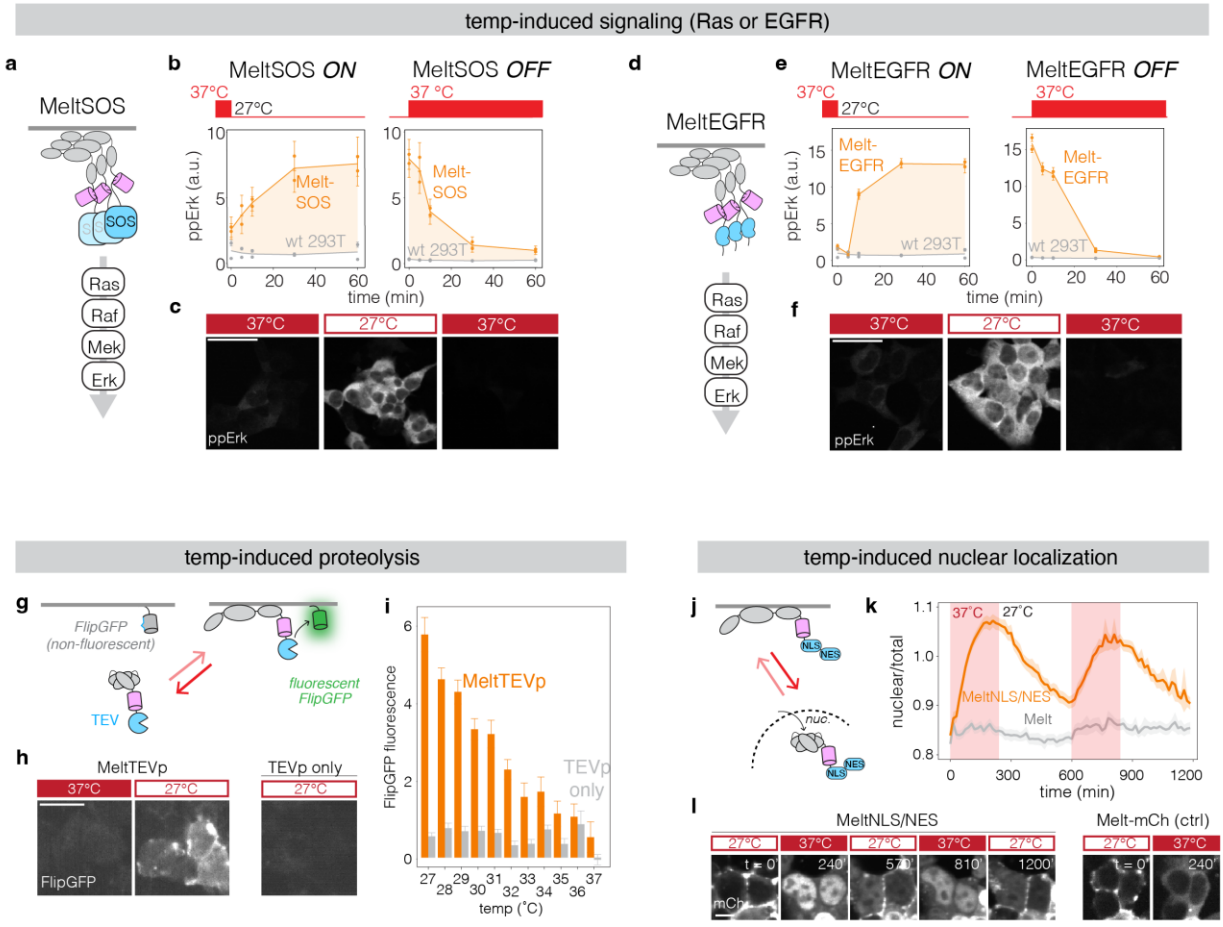

Figure 8: Thermal control over diverse intracellular processes using Melt.

A) Schematic of thermal control of Ras-Erk signaling by membrane recruitment of the SOS2 catalytic domain (MeltSOS). B) Thermal activation and inactivation of Ras as assayed by immunofluorescence for activation of the downstream Erk kinase (phospho-Erk, or ppErk). Data points represent the mean +/- 1 SEM of ~500 cells. C) Representative images of ppErk immunofluorescence from MeltSOS-expressing cells cultured at the indicated temperatures for 24 hours, 1 hour, and 1 hour, respectively. Scale bar = 40 μm. D) Schematic of thermal control of EGFR receptor signaling by membrane recruitment and clustering of the EGFR intracellular domain (MeltEGFR). E) Thermal activation and inactivation of EGFR, assayed through immunofluorescence for ppErk. Each data point represents the mean +/- 1 SEM of ~500 cells.

F) Representative images of ppErk immunofluorescence from MeltEGFR cells cultured at the indicated temperatures for 24 hours, 1 hour, and 1 hour, respectively. Scale bars = 40 μm. G) Schematic of thermal control of proteolysis with MeltTEVp. At low temperatures, MeltTEVp translocates to the membrane where it cleaves a membrane-bound fluorescent reporter of proteolysis (FlipGFP). H) Representative images of FlipGFP fluorescence in cells expressing MeltTEVp or TEVp cultured at 37°C or 27°C for 24 hr. Scale bars = 20 μm. I) Quantification of FlipGFP fluorescence in cells expressing either MeltTEVp or TEVp cultured at the indicated temperature for 24 hours. Each bar represents the mean +/- 1 SEM of ~1000 cells, normalized between negative and positive controls at each temperature. J) Schematic of thermal control of nuclear translocation with MeltNLS/NES. K) Quantification of nuclear localization MeltNLS/NES and Melt-mCh exposed to cycles of 37°C and 27°C. Traces represent the mean +/- 1 SEM of ~1000 cells. See Methods for details on quantification of nuclear localization. L) Representative images of nuclear localization of MeltNLS/NES and Melt-mCh at the temperatures/timepoints found in (K). Scale bar = 10 μm.

Melt temperature sensing and dynamic range is tuneable

The utility of Melt in mammals will depend on its ability to induce a strong change in localization in response to temperature, as well as on its ability to switch near mammalian body temperature (~37°C). We thus sought to tune these properties. To increase the magnitude of membrane translocation, we tested whether short polybasic (PB) peptides could strengthen the electrostatic molecular interactions that mediate BcLOV4 membrane binding[19,72] (**Figure 9A,B)**. We chose two well-characterized PB domains from the STIM1 and Rit proteins, which can enhance membrane-binding of unrelated proteins[20]. End-to-end fusions of Melt to the STIM, tandem STIM (STIM2X), or Rit domains all increased the magnitude of membrane binding at 27°C, in increasing order of strength (**Figure 9C,D**).

Although PB domains provided a large increase in steady-state membrane binding at 27°C, they provided only a mild increase in thermal switch point to ~32°C, only 1-2 degrees higher than the original Melt (**Figure 9D).** We achieved a more substantial increase through the fortuitous discovery that the C292 residue plays an important role in defining the Melt thermal response. In wt BcLOV4, C292 is thought to form a light-dependent bond with a flavin mononucleotide cofactor that underlies the BcLOV4 photoresponse[19]. Although Melt translocation does not respond to light (**Figure 6G)**, introduction of a C292A mutation dramatically increased its membrane association not only at 27°C, but also at 37°C where the original Melt was fully dissociated **(Figure 9E-H**). As before, addition of the STIM PB domain further increased membrane association strength at these higher temperatures. Importantly, both C292A variants retained temperature sensitivity and dissociated from the membrane at 41-42°C, with a thermal switch point of 36.5 and 39.5°C for the C292A and C292A/STIM variants, respectively (**Figure 9H**). Because these Melt variants can exist in one state at 37°C and another at 41/42°C, they are thus both potentially suitable for heat activation within mammalian tissues, with distinct levels of membrane binding and dynamic range that could each be optimal for certain applications. These variants also included a truncation of 96 amino acids from the N-terminal of BcLOV4, which we found expendable, consistent with previous results[19]. Collectively, our work presents four Melt variants with a range of thermal switch points between 30°C and 40°C, covering temperatures suitable for actuation in cells from a broad range of species. We adopted a nomenclature for these variants that reflects these switch points: Melt-30, Melt-32, Melt-37, and Melt-40.

We tested the ability of the higher switch-point Melt variants to actuate post-translational events between 37 and 42°C. MeltEGFR driven by Melt-37 showed strong Erk activation at 37°C and only baseline levels at 40-41°C (**Figure 9I,J**). Erk activity could be stimulated repeatedly over multiple heating/cooling cycles as indicated by the ErkKTR biosensor, which

translocates from the nucleus to the cytoplasm upon Erk activation (**Figure 9K,L**)[73]. MeltSOS-37 could also stimulate Erk activity but only at <~37°C, potentially reflecting a requirement for higher levels of membrane translocation relative to MeltEGFR.

Melt-37/40 could also regulate proteolysis and protein translocation. Melt-40 fused to TEVp showed strong proteolysis and FlipGFP activation at 37°C, with markedly reduced activity at 41°C (**Figure 9M-O**). These results further highlight that although the general thermal response properties are dictated by the specific Melt variant, the precise thermal switch point of the downstream process can be influenced by the specific fusion partner or the downstream process itself. Melt-40 also regulated membrane-to-nuclear translocation within the well-tolerated 37-41°C temperature range (**Figure 9P**). Fusion to a C-terminal SV40 NLS and Stradα NES allowed strong membrane sequestration at 37°C, and fluorescence became enriched in the nucleus upon heating to 41°C (**Figure 9Q,R**). As before, translocation was partially reversible on the timescales tested and could be cycled through repeated rounds of heating and cooling (**Figure 9Q,R**).

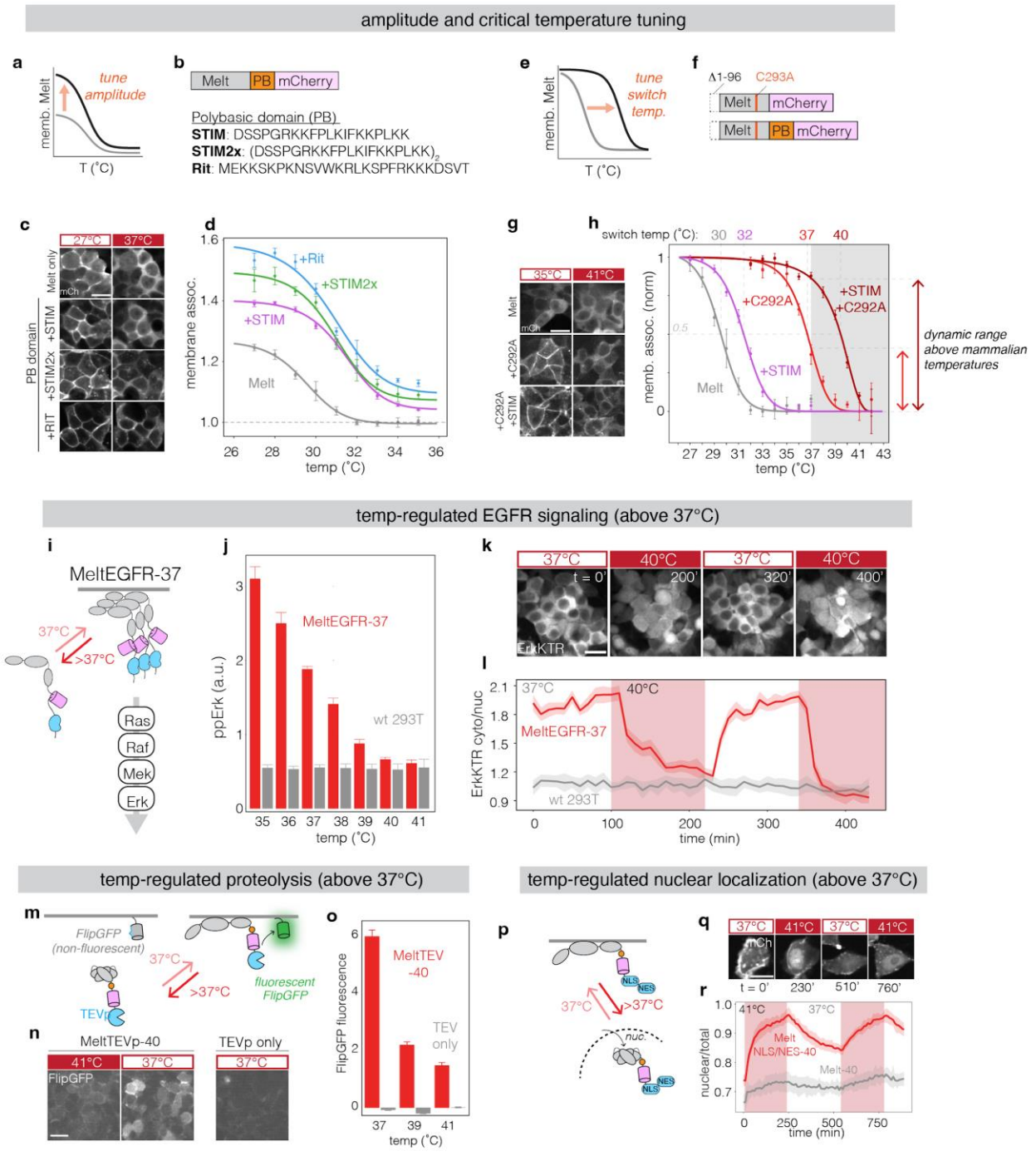

Figure 9: Tuning of Melt membrane binding and thermal switch point allows application of Melt-based tools in mammalian temperature ranges.

A) Tuning the amplitude of Melt membrane association. B) Polybasic (PB) domains from the STIM or Rit proteins were fused to Melt to test their ability to increase Melt membrane binding strength. C) Representative images showing stronger membrane binding (higher membrane/cyto ratio) of Melt fused to PBs compared to Melt alone. Melt constructs were stably expressed in HEK 293T cells and are shown after 24 hrs of culture at 27°C and after subsequent heating to 37°C for 6 hrs. Scale bar = 20 μm. D) Quantification of steady-state membrane association of Melt-PB fusions after culture at indicated temperatures for 12 hours. Data represent mean +/- 1 SD of three wells with ~200 cells quantified per well. Dashed line represents membrane association levels of soluble mCherry. E) Tuning Melt switch-point temperature for use within temperature ranges relevant for mammals, between 37°C and 42°C. F) Schematic of Melt with a C292A mutation with and without STIM PB domain. G) Representative images of membrane localization of Melt, Melt(C292A), or Melt(C292A)+STIM fusion at 35°C for 24 hours and subsequent culture at 41°C for 6 hours. Scale bar = 20 μm. H) Quantification of steady-state membrane binding (14 hrs) of Melt variants between 27 and 42°C. Data represent mean +/- 1 SD of three wells with ~500 cells quantified per well. Data are normalized between min and max values for each construct. Unnormalized traces can be found in Figure 9D. I) Thermal control of EGFR at and above 37°C using Melt-37. J) Immunofluorescence quantification of pathway activation in HEK 293T cells stably expressing MeltEGFR-37. Cells were incubated at indicated temperatures for 75 min before fixation. Bars represent mean +/- 1 SD of three wells with ~1000 cells quantified per well. K) MeltEGFR-37 activation visualized through the live-cell ErkKTR reporter. Nuclear depletion of ErkKTR indicates Erk activation while nuclear enrichment indicates Erk inactivation. Scale bar = 10 μm. L) Quantification of ErkKTR activity (cyto/nuclear ratio) in HEK 293T cells expressing MeltEGFR-37 or wt cells. Traces represent mean +/- 1 SD of ~15 cells per condition. M) Control of proteolysis at mammalian temperatures with MeltTEVp-40. N) Representative images of

FlipGFP signal in cells expressing MeltTEVp-40 or TEVp after incubation at the indicated temperatures for 24 hours. Scale bar represents 10 µm. O) Quantification of FlipGFP signal in fixed cells expressing MeltTEVp-40 or TEVp cultured at the indicated temperatures for 24 hours. Each bar represents the mean +/- 1 SEM of ~1000 cells. Y-axis represents mean fluorescence subtracted by the signal of TEVp-negative cells. P) Control of nuclear translocation at mammalian temperatures with MeltNLS/NES-40. Q) Representative images of nuclear translocation. Scale bar = 20 µm. R) Quantification of nuclear localization of MeltNLS/NES-40 or Melt-40-mCh after exposure to cycles of 37°C and 41°C (red) in HEK 293T cells. Traces represent the mean +/- 1 SEM of ~1000 cells.

Melt for long term cell decision making

We then asked whether Melt variants could be used to regulate cellular-level behaviors at and above 37°C. We first sought to control cell shape changes through the control of actin polymerization. We fused Melt-37 to the DH-PH domain of Intersectin1 (MeltITSN1-37), an activator of the Rho GTPase Cdc42 that has previously been actuated through optogenetic recruitment[74], including with BcLOV4[51,75] (**Figure 10A**). When cooled from 41°C to 37°C, HEK 293T cells expressing MeltITSN1 showed rapid and dramatic expansion of lamellipodia and cell size, consistent with Cdc42 activation[76] (**Figure 10B**). Changes in cell shape could be reversed and re-stimulated over multiple cycles of cooling and heating (**Figure 10C**), showing similar magnitude of shape change in each round (**Figure 10D**). By comparison, temperature changes had no effect on cell shape in cells that expressed Melt-37 without the ITSN1 DH-PH domain.

As a second example, we asked if Melt could be used for thermal control of cell death. Cell death can be achieved by regulated clustering of effector domains of caspase proteins[77]. We fused Melt-37 to the effector domain of caspase-1 (MeltCasp1-37, **Figure 10E**), and we measured cell death upon changes in temperature (**Figure 10F**). By contrast, lowering of

temperature to 34°C led to morphological changes within minutes, followed within hours by blebbing and cell death, indicated by both morphology and Annexin V staining (**Figure 10G,H**). ThermoPlate scanning coupled with live cell imaging of Annexin V revealed cell death induction even when shifting temperature by only 1°C (from 38°C-37°C), and the magnitude of cell death increased with larger temperature shifts (**Figure 10I,J**). No death was measured in cells expressing Melt-37 without the caspase effector.

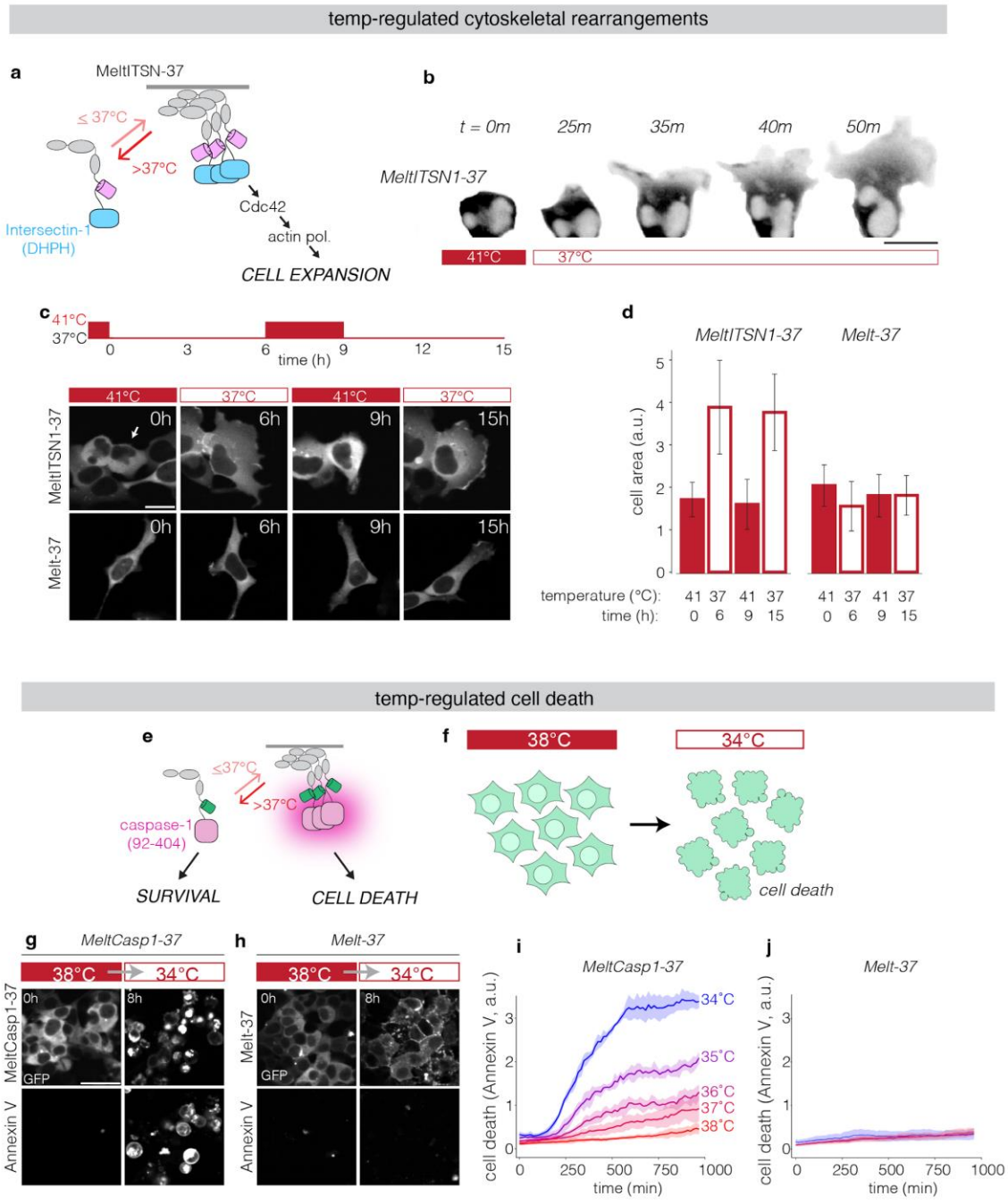

Figure 10: Thermal regulation of cell fate using Melt

A) Control of Cdc42 activity and cell shape through recruitment of the DHPH domain of ITSN1 to the membrane. B) Representative images of cell shape changes in response to temperature control in a HEK 293T cell transiently expressing MeltITSN1-37. Upon reduction of temperature

from 41°C to 37°C, cells show rapid formation of membrane extensions and dramatic increase in size. Scale bars = 20 µm. C) Cell shape changes are reversible and repeatable over several hours of stimulation. Representative images of HEK 293T cells transiently transfected with MeltITSN1-37, cultured at 41°C and exposed to multiple rounds of heating and cooling at the times and temperatures indicated. Scale bars = 20 µm. D) Quantification of cell area of cells expressing either MeltITSN1-37 or Melt-37 after repeated cooling and heating. Bars represent the average cell size of 15 cells +/- 1 SD. E) Thermal control of cell death through regulation of caspase-1 clustering (MeltCasp1-37). F) MeltCasp1-37 induces cell death upon lowering temperature below 37°C. G) Representative images of cells expressing MeltCasp1-37 (G) or Melt-37 (H) before and after exposure to 34°C for 8 hours after culture at 38°C for 24 hours. Bottom panels of (G,H) show Annexin V-647 staining, which indicates cell death. Scale bars = 40 µm. I) Quantification of Annexin V intensity in MeltCasp1-37 and Melt-37 cells over time at the indicated temperature after prior culture at 38°C for 24 hours. Plots represent the mean +/- SEM of per-image Annexin V fluorescence divided by total GFP fluorescence (to account for cell density) across 4 images. See Methods for quantification details. All images/data in this figure were collected using transient expression of Melt constructs in HEK 293T cells.

Non-invasive subcutaneous control of biochemistry in-vivo

Finally, we asked whether Melt could control cell behavior in animals in a spatiotemporally defined manner by testing its ability to induce cell death in mouse xenografts of human cancer cells. H3122 lung cancer cells expressing MeltCasp1-37 and firefly luciferase rapidly underwent cell death in < 3hrs after cooling from 37-25°C in culture (**Figure 11A**). We then injected these cells into both flanks of immunodeficient NSG mice and, 48 hr after injection, we cooled the tumor on one flank while leaving the contralateral tumor untreated (**Figure 11B**). Cooling (45 min at 5°C followed by 45 min at 15°C) was performed by topical application of a

custom thermoelectric cooling device that maintained programmable feedback-controlled temperature (**Figure 11C**). Luciferase imaging revealed ~80% reduction of tumor cells in the cooled flank relative to the uncooled flank only 3 hr after cooling. No reduction of tumor cells was observed in xenografts lacking MeltCasp1-37 (**Figure 11D,E,F**). Cooling over subsequent days gave no further reduction in luciferase signal, suggesting that the initial cooling maximally eliminated cells (**Figure 11G**). Thus, Melt can control cell behavior in mammals in a spatiotemporally defined manner using a non-invasive temperature stimulus.

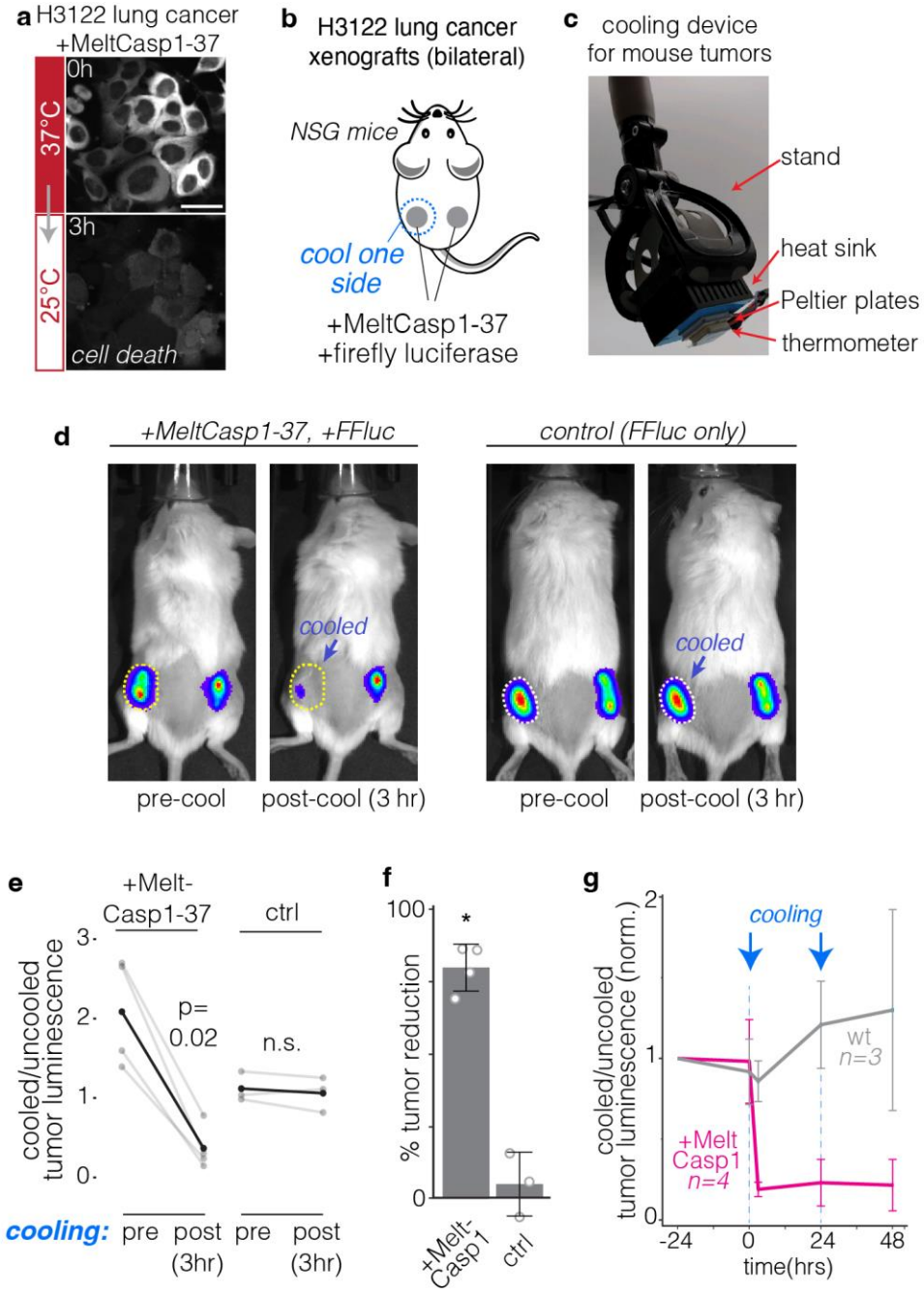

Figure 11: Thermal control of Melt and cell fate in animal models

A) H3122 cancer cells expressing MeltCasp1-37 show rapid cell death within 3 hrs after cooling. Scale bar represents 40µm. B) Bilateral tumor model to test spatiotemporal control of MeltCasp1-37 in vivo. Mice were injected on both flanks with H3122 cells expressing

MeltCasp1-37 and firefly luciferase or luciferase only (control). 48 hrs post injection, cooling was applied locally to one flank. C) Device for programmable cooling of xenografts. A Peltier element cools the outward-facing surface, which provides localized topical cooling when applied to the mouse. A thermistor allows real-time monitoring and feedback control of temperature. D) Representative images of mice before and after cooling. Cold treated tumors showed dramatic reduction in luciferase signals relative to uncooled tumors, but only for tumors expressing MeltCasp1-37. Cooling protocol: 45 minutes of 5°C followed by 45 minutes of 15°C. E) Quantification of (D). Light grey: individual mice. Black: mean. Significance determined by a one-sided Wilcoxon signed-rank test. F) Tumor reduction was obtained by calculating the change in luminescence ratio (cooled/uncooled) as a result of cooling. N = 3-4 mice, bars = mean +/- SD. p = 0.028 by one-sided Mann-Whitney test. G) Relative luminescence of cooled vs uncooled tumors over multiple days, with treatment repeated at 0 and 24 hrs. Traces represent the mean +/- 1 SD of 3-4. Values normalized to the first day of imaging.

Discussion

Here we have described a modular and tunable protein that permits thermal control over a range of molecular and cell-level behaviors. By locking the naturally light- and temperature-sensitive BcLOV4 into its “lit” state, we generated the purely thermoresponsive Melt whose membrane association and clustering can be regulated with a small temperature change (<4°C). Tuning this thermal response further allowed us to generate multiple variants (Melt-30/32/37/40) whose activation switch points could be shifted within the 30-40°C range. These variants allowed temperature-inducible control of signaling, proteolysis, and subcellular localization, including between 37°C-42°C, a critical range for thermal control within mammals. Finally, we showed that Melt can provide thermal control over cell and tissue-level behaviors by changing cell size/shape and cell death, both in vitro and in vivo.

Our engineering efforts provide insight into how the wt BcLOV4 protein senses both light and temperature. Successful isolation of the BcLOV4 thermal response from its light response confirms the distinct molecular nature of these two behaviors, as previously speculated[61]. At the same time, the light and temperature responses are intertwined, since mutation of the C292 residue in the LOV domain, which mediates photo-responsiveness, dramatically shifted the thermal switch point of Melt (**Figure 10E**). Further mechanistic and structural work will be required to fully understand the molecular basis for BcLOV thermal sensitivity, potentially allowing optimization of Melt properties including speed of response and degree of reversibility, and will shed light on how the photosensing and thermosensing elements of BcLOV4 interact. These latter studies will additionally provide insight for how to engineer novel multi-input proteins that can perform complex logic in response to user-defined stimuli.

Multiplexed control of sample temperature allowed us to systematically characterize new Melt variants, ultimately resulting in variants with switch-points ranging from 30-40°C. Because optogenetic BcLOV4 works in mammalian cells but also in systems that are cultured at lower temperatures like yeast, flies, zebrafish, and ciona[19,49,50,61,75,78], we anticipate that all Melt variants will find use across these and similar settings. Our work also highlights the utility of having multiple variants in hand to optimize specific downstream applications. We found on multiple occasions that the precise thermal response profiles depended not only on the specific Melt variant but also on both the effector and downstream process under control, thus requiring empirical validation for each use case and biological context. Optimization can be performed by testing other Melt variants, or by generating new ones through additional mutations or modifications (e.g. polybasic domains) similar to the ones we describe.

Melt dramatically expands the range of molecular and cellular events that can be controlled by temperature and, in mammalian cells, allows thermal control with lower potential for heat stress relative to the few existing approaches. Melt provides an orthogonal input control

that can be used in conjunction with—or instead of—existing technologies based on light or chemicals, and it affords unique potential for actuation of proteins and cells in animals, opening exciting avenues across biotechnology and biomedicine.

CHAPTER 3: DEVICES FOR HIGH-THROUGHPUT TEMPERATURE SCREENING

Portions of this chapter was previously published/is in press as:

William Benman et. al. *"Multiplexed dynamic control of temperature to probe and observe mammalian cells."* bioRxiv 2024.02.18.580877; doi: https://doi.org/10.1101/2024.02.18.580877

W.B. was the primary author of this manuscript.

Background

During the development of Melt, we found that screening a protein's response to temperature was severely limited using existing technology for temperature control of biological samples. This limitation affected not only our work, but also the study of many temperature sensitive phenomena throughout biology. Temperature plays important roles in the function and control of biological systems. In humans, core temperature is narrowly maintained around 37°C and, although temperature can rise during infection, the febrile response is also tightly controlled to remain below ~41°C[79]. In the biosciences, temperature can be harnessed as a non-invasive perturbation, for example with temperature-sensitive protein mutants that provide conditional knockdown of proteins[31–33]. Separately, heat-shock promoters can allow expression of custom transgenes in response to a brief increase in temperature. Such technologies can control gene expression in model organisms[80] and, because heat effectively penetrates opaque tissues, also provide remote control of engineered cells within mammals[22,26,27]. Exposing mammalian cells to temperatures above ~42°C induces heat shock, which can be toxic over extended periods. This response has been harnessed for cancer therapy, where thermal ablation of tumors is a common, minimally-invasive treatment strategy[81].

Despite its importance, there are relatively few experimental methods to systematically manipulate temperature. Incubators can be set to desired temperatures, but changes in temperatures are slow, challenging studies of phenomena that occur over fast (~minutes)

timescales. Incubators are also expensive, have a large footprint, and allow only one temperature to be tested at a time. Commercial devices such as the CherryTemp or VAHEAT are similarly limited in throughput. Thermocyclers can be used to specify multiple temperatures simultaneously[35], but these are not compatible with long term cell survival or simultaneous imaging. The current lack of methods for microscope-compatible temperature modulation in microwell plates limits our understanding of biological responses to temperature changes and hinders the engineering of thermally-controllable biological systems.

We address this gap with the thermoPlate, a device for programmable heating and thermometry of samples in 96-well plates. The thermoPlate allows heating of individual wells with arbitrary temperature profiles and is compatible with both live-cell microscopy and standard cell culture incubators. We characterize thermoPlate performance, finding accurate heating across the plate to < 0.1°C of the desired set point. We also present a model that predicts heat diffusion across the sample plate, allowing the user to rapidly test the feasibility of arbitrary desired heating programs *in silico*. We then harnessed the utility of the thermoPlate to characterize the rapid temperature-dependent phase-separation of an elastin-like polypeptide (ELP). Finally, we examined the dynamics of stress granule (SG) formation in response to graded levels of heat stress. We found that SGs form but spontaneously dissolve due to the formation of biochemical memories of stress, which depended on both the timing and intensity of heat stress.

thermoPlate96 design and use

The thermoPlate maintains a desired temperature by continuous deposition and measurement of heat in each well of a 96-well plate (**Figure 12A**). This is achieved with a custom-designed circuit board that accommodates a pair of thermistors in each of 96 positions in the format of a 96-well plate. A thermistor is a resistor whose resistance changes as a

function of temperature, thus enabling its common use as a thermometer (“reader”). However, thermistors can also deposit heat when sufficient current is passed through them (“heater”). By pairing one reader and one heater thermistor in each well, the thermoPlate achieves independent measurement and heating of all 96 wells (**Figure 12A, B**). To operate, the user uploads the desired heating protocols to the on-board Arduino microcontroller. With the set point and temperature of each well, the Arduino implements proportional-integral-derivative (PID) feedback control, adjusting the current of each heater to reach and maintain the sample at the desired set point for every well (**Figure 12C**). The thermoPlate sits atop a 96-well culture plate to which it is mated with a 3D printed adapter (**Figure 12D**). The thermoPlate can operate in standard cell culture incubators. Alternatively. when the culture plate has a transparent bottom, this assembly is also compatible with live cell imaging using an inverted microscope. The thermoPlate can run in a standalone format but can also be connected to a computer to view real-time readouts of the current well temperatures.

Multiplexed temperature control requires consistent, calibrated readings between each of the 96 readers. We characterized the variability in temperature readings in a fully-assembled thermoPlate in a cell culture incubator that was set to one of 5 temperatures between 26-45°C, with the true temperature verified by two digital thermometers. While the average error between thermoPlate and true temperature increased slightly at higher temperatures, we observed a consistent pattern of variability between wells (SD ~ 0.26°C) (**Figure 12E**). From these results, we derived adjustment factors for each well that corrected readings to within 0.1°C of the true temperature across all temperatures, with a standard deviation of 0.06°C between wells in subsequent experiments (**Figure 12E**).

We next tested the thermoPlate’s ability to control prespecified temperatures, with temperature measured by the calibrated reader thermistors. 15 wells were set to simultaneously maintain temperatures ranging from 28°C to 42°C (3-17°C above ambient) in 1°C increments

(**Figure 12F**). After a rapid approach and equilibration at the designated set point, each well maintained its temperature with high accuracy (average error of 0.04°C from set point) and precision (average SD of 0.05°C within individual trace) over 15 hrs of operation (**Figure 12F**). Moreover, temperatures could be dynamically toggled between multiple setpoints, returning to the desired temperature with high fidelity (at steady state: average error of 0.07°C, average within-trace SD = 0.06°C) (**Figure 12G**).

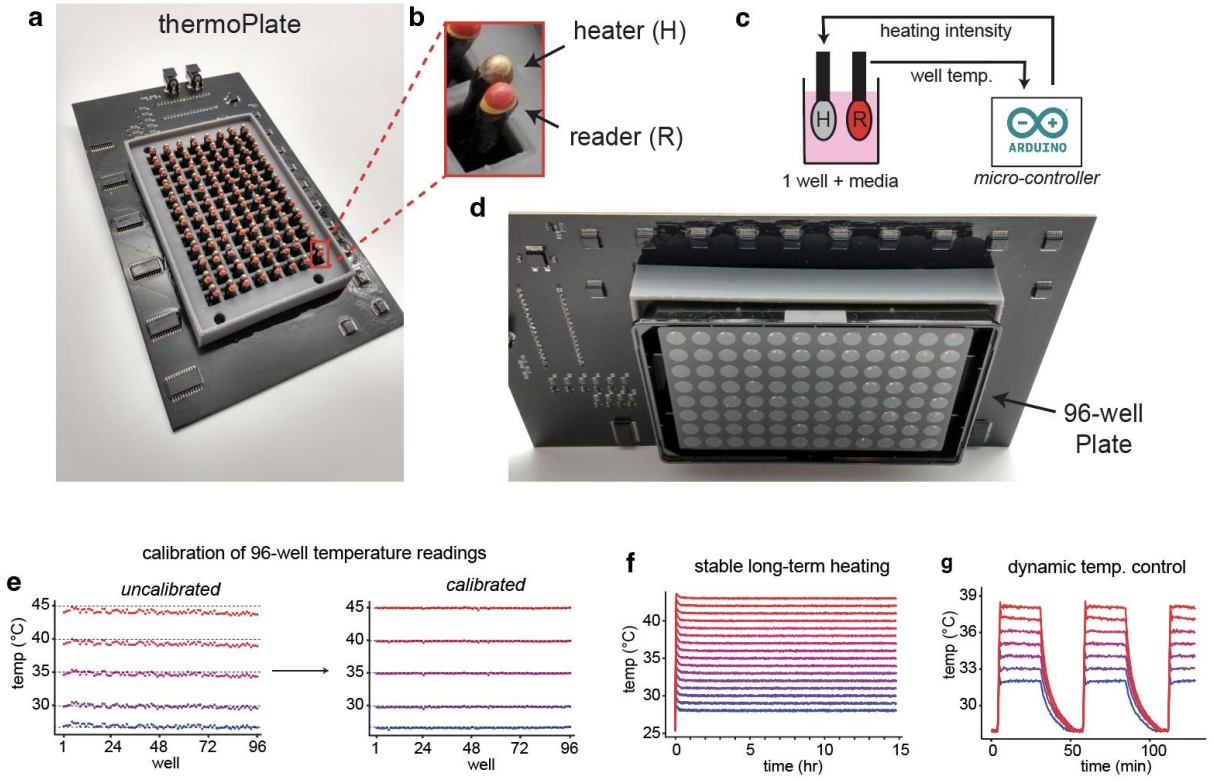

Figure 12: Design and use of the thermoPlate for simultaneous, independent temperature control in 96 well plates.

A) Image of a fully assembled thermoPlate device. B) Enlarged image of a single heater/reader pair, which regulates the temperature of a single well of a 96 well plate. C) An Arduino takes readings from a reader and dynamically adjusts the duty ratio of the heater using PID feedback

control. D) Image of a thermoPlate inserted into wells of a 96 well plate. E) Raw readings taken from the reader of each well when placed in a cell culture incubator set to various temperatures before and after calibration. Color and dashed lines represent the incubator temperature. See Methods for details on calibration. F) Traces showing 16 wells that were set to 16 different temperatures in 1°C increments (28-43°C) with an ambient temperature of 25°C for 15 hrs. G) Dynamic temperature control in multiple wells over multiple temperatures. 7 wells were heated to different temperatures for repeated cycles of 30 minutes of heating followed by 10 minutes of cooling to 28°C, with an ambient temperature of 25°C.

Characterization of thermoPlate performance

We next characterized key operational features of thermoPlate heating, including its range, accuracy, heating/cooling speed, and overshoot. We devised an experiment where the thermoPlate would sequentially heat each well from 3°C above ambient temperature to a prespecified higher temperature for 20 minutes, followed by cooling back to 3°C above ambient. Note that because the thermoPlate has no active cooling, in most experiments the baseline (lowest) experimental temperature should be set to higher than ambient to allow rapid cooling to—and maintenance of—this desired low temperature. **Figure 13A** demonstrates the above described experiment for heating through $\Delta T = 10°C$. All wells experienced this heat pulse with high consistency between wells (**Figures 13A,B**). From this type of experiment, we could systematically quantify error (difference between the temperature and the set point after 20 minutes), rise/fall time (the time until temperature reached 99% of the target temperature), and overshoot/undershoot (difference between the maximum/minimum and setpoint).

To quantify performance as a function of heating magnitude, we chose 11 wells distributed across the plate and repeated the above experiment with heating of either 5, 10, 15, or 20°C above ambient, with each well heated sequentially (**Figure 13C**). While all wells

reached their target temperature for up to ΔT = 15°C, only some wells could reach ΔT = 20°C within 20 minutes. The rate at which a well approached ΔT = 20°C was highly dependent on its position on the plate, with corner wells approaching 20°C more rapidly than center wells**.** This variability in heating speed likely arises because of differences in heat diffusion in different parts of the plate, with higher numbers of neighbor wells acting as a larger heatsink that limits heating. Rise/fall times were 2 min for ΔT = 5°C and 4 min for ΔT = 10°C, with increasing variability between wells with increasing ΔT (**Figure 13D**). However, error (0.05-0.15°C) and overshoot/undershoot (0.1-0.3°C) were minimal and did not correlate with ΔT.

Although heat diffusion limited the heating range of individual wells, it could also be harnessed to boost heating within groups of wells. We tested this concept by heating either individual wells or groups of 4 or 9 wells to ΔT = 20°C. Although, as before, individual wells struggled to reach this level of heating, wells in a 3x3 matrix rapidly equilibrated to this high set point (**Figure 13E**). Grouped wells achieved a faster approach to high temperatures at the expense of small increases in error (0.15-0.2°C) and overshoot (~1°C) (**Figure 13F**). In sum, the thermoPlate can reliably and rapidly achieve heating of up to ΔT = 15°C in individual wells and can also be programmed to achieve ΔT >20°C with appropriate arrangement of the heated wells.

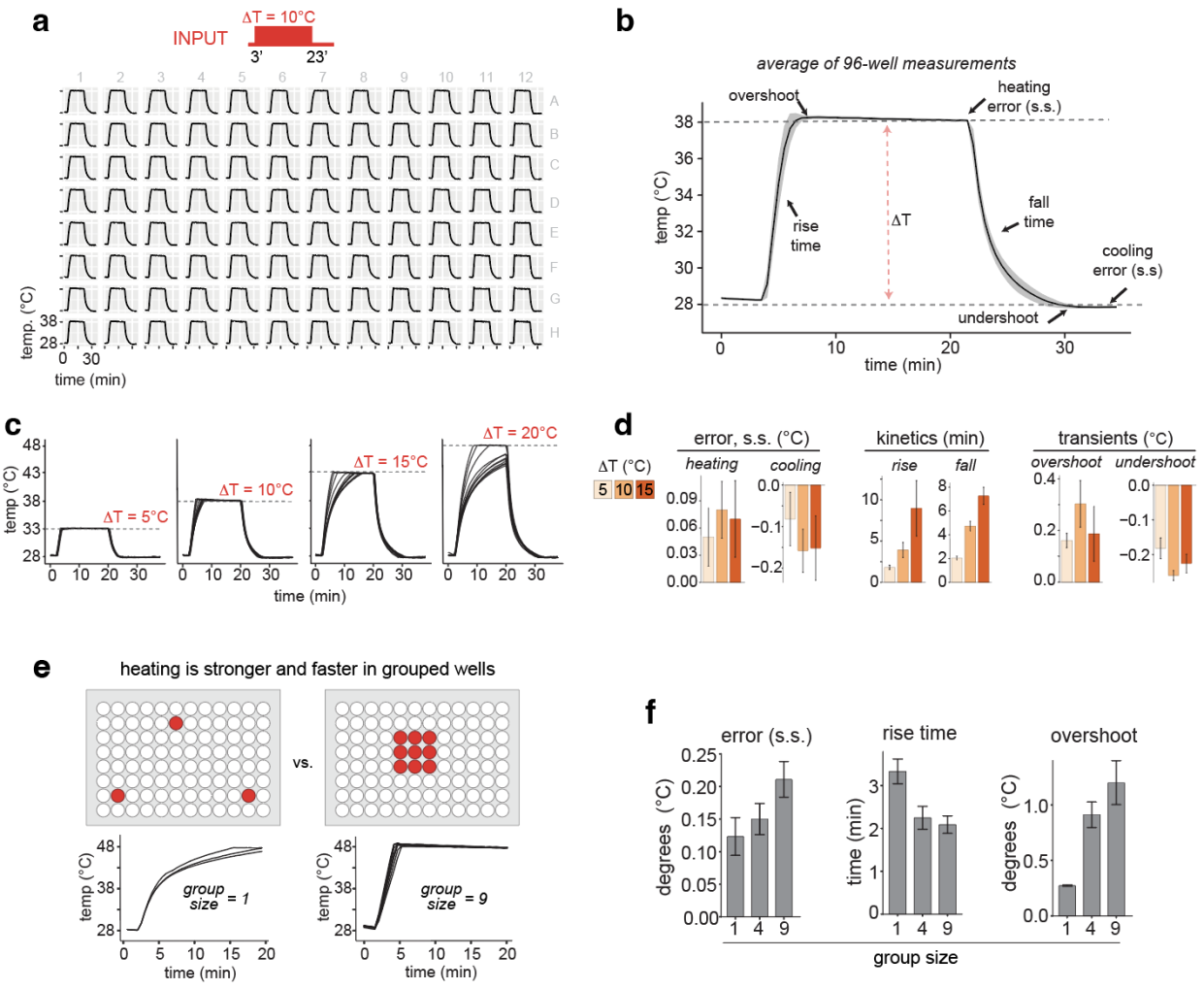

Figure 13: Characterization of thermoPlate heating and cooling

A) Temperature profile of each well heated with a 20 min pulse of 10°C. Wells were heated sequentially. B) The mean of all 96 traces from (A) labeled with key metrics of thermoPlate performance. Heating error = difference between the measured and set point temperature at 20 minutes. Rise time = duration at which temperature reached 0.5°C of the desired temperature. Overshoot = difference between maximum measured and set point temperature during heating. Cooling error, fall time, and undershoot represent the same parameters during the cooling phase. Error ribbons = 1 SD. s.s. = steady state. C) Heating each of 12 wells through 5, 10, 15, or 20°C for 20 minutes and then cooling to 28°C (ambient = 25°C). D) Mean of each

performance metric from (C). Error bars represent = SD. E) Heating amplitude and speed can be increased by heating groups of wells. Wells were programmed to heat by ΔT = 20°C as either single wells or a group of 9 wells. F) Performance metrics of heating as a function of well grouping. Wells were heated by ΔT = 10°C. Data represents mean +/- SD from 3-9 wells.

Generating a model of thermoplate heat diffusion

Heat diffusion constrains the heating protocols that can be run simultaneously because it places limits on the temperature differential between two neighboring wells. For example, a well heated to 15°C above ambient will diffusively heat its neighboring wells by ~10°C, placing a lower limit on the possible temperatures of those neighbors. As the number of wells in use increases, it becomes increasingly challenging to predict whether a desired protocol is achievable, particularly when dynamic heating protocols are desired.

We thus created a model of heat diffusion in 96-well plates to allow users to rapidly assess the feasibility of particular heating programs. We implemented an explicit finite difference approximation of a modified heat equation. This model simulates dynamic heat stimuli and calculates the rate of heat spread through each well of the plate over time. Unlike the classical heat equation, our model has 6 (vs 1) parameters that describe the rate of heat spread. These additional parameters account for observed differences in heat spread across different contexts, for example in edge wells vs center wells (**Figure 14A**). These parameters also accounted for small asymmetries around heated wells (left vs right, top vs bottom) likely due to asymmetric positioning of the electrical components.

To fit the model, we generated eight sets of training data where different sets of wells (1-12 wells) underwent dynamic heating/cooling programs, with temperature changes of 1-15°C over durations of up to 90 min (**Figure 14B**). These training experiments were designed with increasing levels of complexity, from simple heating of one well (Dataset 1) to more complex,

dynamic heating of 12 wells arranged both individually and in groups (Dataset 8). The model was parameterized for each training set by minimizing the root mean squared error (RMSE). These 8 parameter sets were then averaged to create a final set of parameters that describe thermoPlate behavior. We validated the model using Leave-One-Out-Cross-Validation, wherein fitted parameters from 7 training sets were averaged and used to predict the 8th dataset, resulting in a mean average error of 0.23°C across all wells and times. Comparing the predictions of the full model vs the data across all data sets, the average error over an experimental run was 0.22°C (**Figure 14C-E**), with error falling within 1°C for > 99% of timepoints and within 0.5°C for > 75% of timepoints (**Figure 14E**), showing close agreement between model and data. Transient spikes in error (1-2°C) could on occasion be observed near wells that experienced a sudden large temperature change (**Figure 14D**).

The predictive power of this model allows users to rapidly test whether particular heating patterns and spatial arrangements are permissible. For this purpose, we created an online interface where users can upload the desired heating protocol and easily simulate and visualize heat generation and spread (**Figure 14F**). The visualization also highlights impermissible temperature set points, allowing the user to modify their experimental design accordingly.

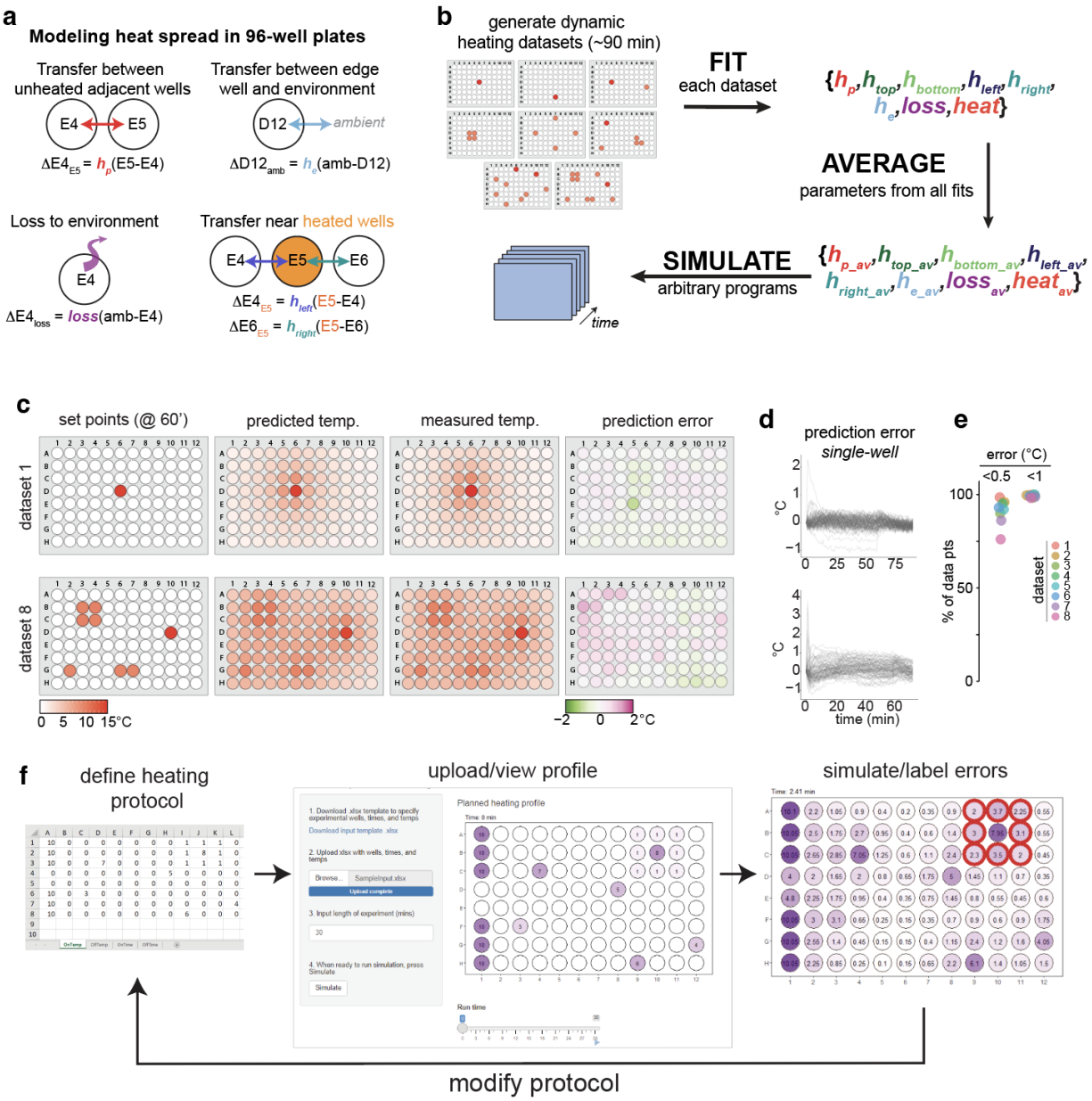

Figure 14: Mathematical modeling predicts the temperature of all wells in a sample plate

A) Diagram of parameters used to model heat diffusion in a 96-well plate that is heated by a thermoPlate. B) Strategy for parameter fitting. 8 parameter sets were fit to 8 separate experiments that spanned a range of wells, temperature, and heating dynamics. Parameters were then averaged across the parameter sets. C) Comparisons of set points, model predictions, actual temperatures, and error between predictions and model for the 60 min time

points of two heating datasets. D) Traces of error (predicted-measured) within each well over the entire duration of two datasets. Each trace represents the error within a single well. E) Summaries of error for each well and time point of each data set. F) A Shiny App GUI allows users to upload heating profiles, review the profiles visually, and simulate heating and heat diffusion during a run. The simulation shows the predicted temperature of all wells and indicates whether any prespecified temperature profiles are unachievable due to thermal diffusion from neighboring wells (red circles in right panel). The user can then adjust and simulate the adjusted protocol until no errors are found.

The thermoPlate allows rapid characterization of thermo-responsive proteins

We first leveraged rapid and dynamic thermal control to characterize phase separation of an elastin-like polypeptide (ELP_{53}), which forms protein condensates in mammalian cells above a critical temperature (**Figure 15A,B**)[82]. ELP condensates form rapidly (~minutes) and over a small temperature range (~1-2°C)[83,84]. We used the thermoPlate coupled with live-cell confocal microscopy to observe ELP_{53} condensation in response to increased temperature between 28-39°C, at 1°C resolution (**Figure 15C**). ELPs condensed rapidly and as a function of temperature, with measurable condensation above 31°C and a ~linear increase in magnitude between 33-38°C (**Figure 15C,D**). We next quantified the speed of ELP formation kinetics, finding that ELP condensation increased within 1 min of heating and reached steady-state within 10 min (**Figure 15E**). Notably, the thermoPlate achieved its target temperatures in <2 minutes, sufficiently fast to observe the slightly slower ELP condensation. The fast and dynamic responses of both the thermoPlate and ELPs allowed us to reversibly toggle ELP phase separation over 45 cycles of heating and cooling (4 min 35°C, 4 min 29°C). ELP condensation and dissolution remained consistent over all cycles, with no decrease in dynamic range, suggesting that such stimulation could be maintained indefinitely (**Figure 15F**).

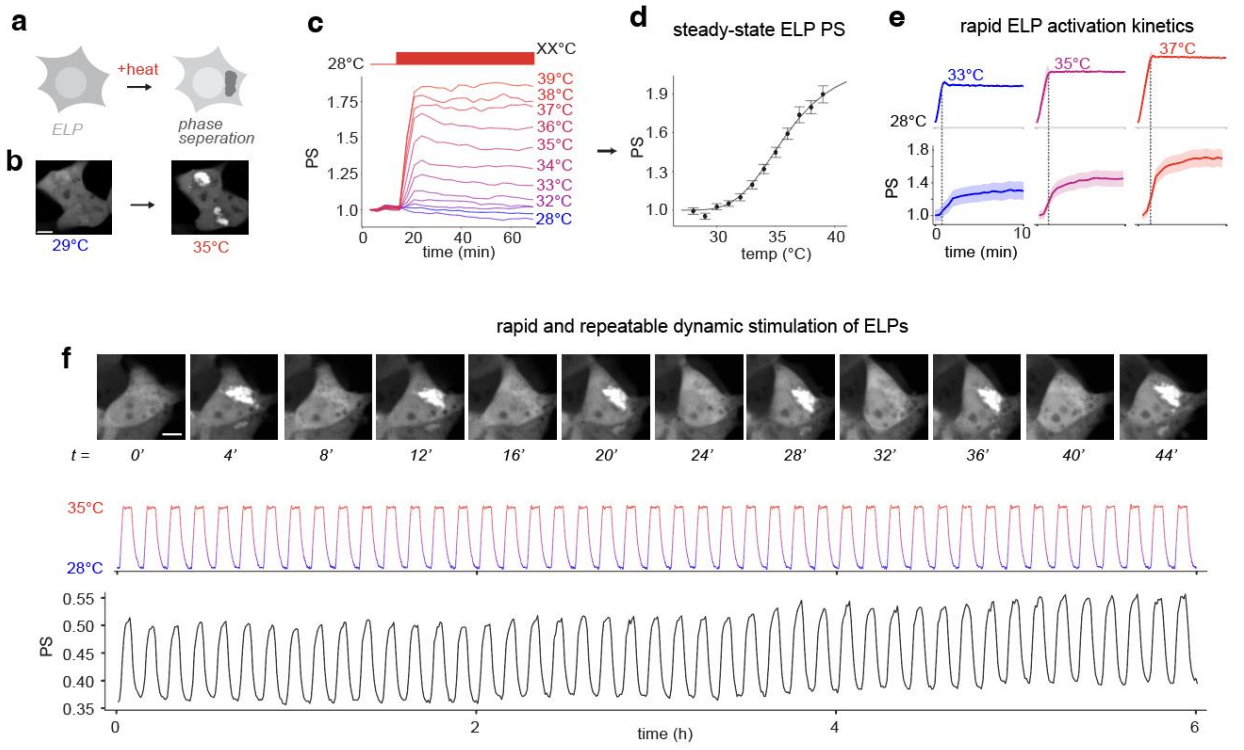

Figure 15: The thermoPlate allows rapid characterization of the phase separation of an elastin-like polypeptide (ELP53).

A) Diagram of ELP phase separation (PS) upon elevated temperature. B) Representative image of ELP phase separation when transition from 29°C to 35°C in HEK 293T cell lines. C) Cells expressing ELP-GFP were exposed to various temperatures for 1 hour while undergoing simultaneous confocal microscopy. Each trace represents the mean of ~500 cells. PS values are normalized to t = 0. See methods for PS quantification. D) The equilibrium PS at each temperature from (C) plotted vs temperature. Each point represents the mean of ~500 cells +/- 1 SEM. PS is normalized to values at 28°C. E) Quantification of the kinetics of ELP PS at 3 temperatures. Traces represent the mean of ~500 cells +/- 1 SEM. PS values are normalized to t = 0. F) Rapid and dynamic control of ELP PS can be maintained indefinitely. Data show 45 cycles of 4 minutes of heating to 35°C followed by 4 minutes at 28°C. The temperature trace represents the mean of 3 wells. PS traces represent the mean of ~1000 cells.

The thermoPlate reveals heat shock “memory” in stress granules

We next applied the thermoPlate to examine native thermal responses of mammalian cells. We focused on the dynamics of stress granule formation in response to heat shock. Stress granules (SGs) are condensates of protein and RNA that form in the cytosol in response to stressors including heat, hypoxia, and oxidation[85]. While the composition and function of SGs in response to heat stress have been studied extensively[86–91], their dynamics are relatively less explored. To observe stress granules, we stably expressed a fluorescent fusion of the SG scaffold G3BP1-mCherry in HeLa cells, and we imaged G3BP1 condensation as a function of time and temperature.

We first asked at what temperature SGs could be observed by exposing cells to constant heat between 41 to 47°C (**Figure 16A**). We found a highly non-linear relationship between temperature and the magnitude of stress-granule formation. Although no SGs were observed at 41°C, SG rapidly formed at 42°C and increased in magnitude at 43°C and 44°C. Surprisingly, maximal SG intensity decreased with progressively further increases in temperature (**Figure 16B-D**). Although cells remained morphologically unperturbed with SGs at 42°C and 43°C over at least 8 hrs, cells heated with 44°C lost cytoplasmic volume and became immobile, with higher temperatures leading to faster onset of this phenotype (**Figure 16C**)**.** In all heating conditions**,** SGs formed rapidly within the first 5 min.

Notably, SG formation was transient across all conditions despite constant heating, and in most cells G3BP1 returned to a diffuse state within several hours of the onset of heat shock (**Figure 16B**). We asked if SG adaptation required constant heat stress or alternatively could form in response to short heat pulses. We examined SG formation in response to periodic 1-hr pulses of heat stress (43.5°C), a pulse duration shorter than the time scale of SG adaptation (**Figure 16B**). Although the SGs formed and dissolved in sync with the first two heating and cooling pulses, SGs largely did not form during the 3rd and subsequent pulses, suggesting that

cells continued adapting to heat stress despite heat not being applied for the entire duration of adaptation (**Figure 16E,F**). Indeed, even though the second heat pulse yielded strong SG formation, SG magnitude began to decrease during this second window, indicating that the first heat pulse influenced SG behavior during the second heat pulse (**Figure 16E**). Collectively, these results show that cells store memories of prior heat exposure that shape future responses to repeated stress.

We next characterized the timescales of this memory formation. We programmed the thermoPlate to apply two pulses of heat stress (43.5°C) separated by varying periods of relaxation at 37°C (**Figure 16G**), and we quantified SG formation during the second pulse. SG formation depended on the interval between pulses in a biphasic manner. Although SGs were prominent during the second pulse after a 1 or 2 hr interval, they were not observed with intervals of 3 and 4.5 hrs. At still longer intervals, SG formation began to reappear on the second pulse. With a 9 hr interval, SG formation during the 2nd pulse resembled that of the first pulse (**Figure 16G,H**). Thus, cellular memory of prior stress was maximal for 3-6 hrs after which the memory began to fade and cells again responded to heat shock as on the first exposure.

Finally, we wondered whether memories of prior heat shock depended on the duration or the temperature of heat shock, or both. We designed a “pump-probe experiment” where we delivered a “pump” of heat stress with variable duration (15, 30, 60 min) and temperature (43-44.5°C), returned to 37°C for 3 hr, and then “probed” SG formation with a subsequent 1 hr of heat shock (43.5°C) (**Figure 16I**). Indeed, memory (suppression of SG formation on the second pulse) depended on both time and temperature of the initial heat shock pump. Suppression of SGs was stronger with increasing temperatures, and the magnitude of suppression increased with increasing pump duration. Notably, even a short 15 min pump was sufficient for measurable SG suppression at higher temperatures (**Figure 16I,J**). Additionally, the rate of dissolution of SGs after removal of the pump pulse depended on the intensity and duration of

heat stress, with slower dissociation in response to longer and more intense heating (**Figure 16I**), indicating a second form of stress memory. This effect could only be observed at or above 44°C heating and could be observed even after a brief 15 min pump duration (**Figure 16K**). In sum, our results indicate multiple mechanisms by which cells can store memories of prior heat stress and demonstrate the utility of the thermoPlate to explore these stress responses efficiently with high precision, throughput, and temporal resolution.

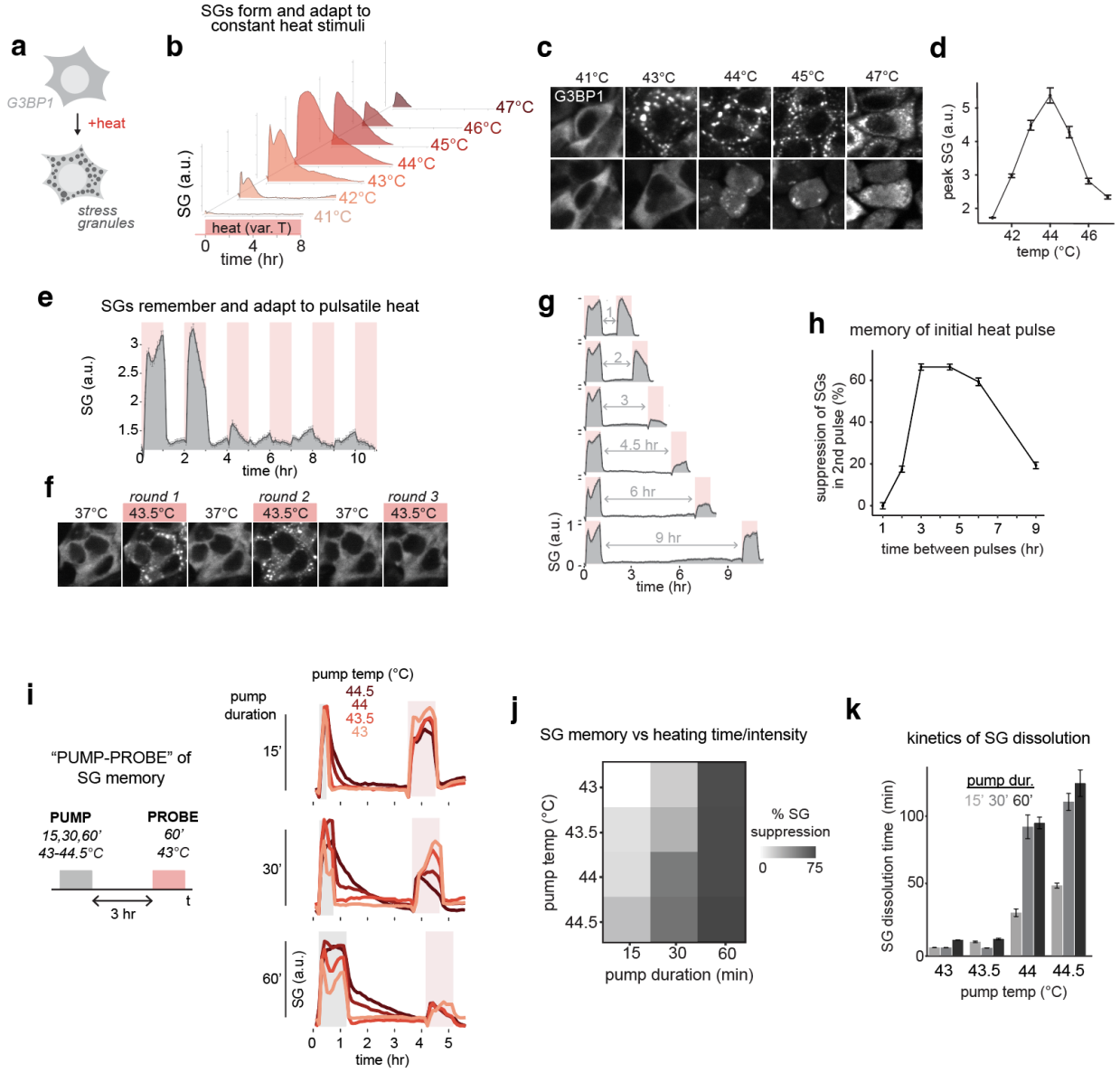

Figure 16: The thermoPlate allows visualization of mammalian heat shock response with high resolution in temperature and time

A) Heat induced stress granule (SG) formation was observed by measuring condensation of G3BP1-mCh in response to time varying temperature changes in HeLa cells. B) SG formation in response to constant heating. Each trace represents mean SG formation from two wells. C) Representative images of experiment in (B). D) Maxima of SG formation across all temperatures tested. E) SG response dynamics in response to pulsatile stimuli. Red bars indicate heating intervals (1 hr at 43.5°C), which were separated by 1 hr intervals at 37°C. F) Interrogating temporal properties of heat shock memories that suppress stress granule formation. Cells were heated for 1 hr intervals (43.5°C) separated by variable intervals at 37°C, and SG formation on the second pulse was measured. G) Cells were exposed to 1hr of 43.5°C and allowed to return to 37°C for various time intervals and then exposed to 1hr of 43.5°C for a second time. SG formation was quantified. H) The degree of suppression of SGs on the second pulse from (G) is quantified as a function of the interval between heat pulses. I) A “pump-probe” experiment to interrogate the effects of temperature and duration of heat shock on SG memory. The temperature and duration of the “pump” heat pulse were varied, and the magnitude of SG formation on a second heat pulse (1 hr, 43.5°C) was measured. J) Quantification of SG memory (suppression during the probe pulse) as a function of pump temperature and duration from experiment in (J). K) Quantification of kinetics of SG dissolution after the pump pulse. Dissociation time was calculated as the time at which SG magnitude dropped 90% from its peak value before adaptation. Data represents mean +/- SD of four replicates.

Discussion

The thermoPlate allows modulation of the temperature of biological samples in a multiplexed and small format that is compatible with both long term cell culture and live-cell

microscopy. After calibration, the thermoPlate achieved its desired set point temperatures rapidly and accurately, with minimal variation between wells, allowing profiling of the response to thermal dynamics with high resolution in temperature and in time. The device is open source and can be assembled by non-specialists in several hours by following the assembly protocols associated with this manuscript, for a total cost of ~$300 in parts. The design files can also be modified to adapt the device for user-specific applications as needed, for example for use in larger well-plate formats.

Heat diffusion constrains the types of heating protocols that can be run simultaneously. Nevertheless, these constraints need not limit throughput. For example, if a sustained temperature sweep is desired, a temperature gradient can be specified across the plate, and all 96-wells can be used simultaneously. For more complex and dynamic patterns, samples must be placed more strategically to allow the samples to heat and cool appropriately. While this is straightforward for a few samples, it becomes more challenging with each additional heated well. For this reason, we developed a model of thermal diffusion that accurately predicts heating dynamics of each well for arbitrary protocols. The user can rapidly simulate a desired protocol in silico and observe whether the intended thermal patterns are permitted within the constraints of thermal diffusion. If they are not, the user adjusts the inputs, simulates, and iterates until a suitable arrangement is reached. We also introduce a web-based GUI for easy access to this model.

The thermoPlate also harnesses thermal diffusion to passively cool the samples. The simplicity of passive cooling is balanced by two additional constraints: 1) potentially slow cooling kinetics and 2) inability to maintain certain wells at ambient temperatures while heating other wells, since over time all wells will increase temperature by a few degrees as heat spreads throughout the plate faster than it diffuses out to the environment. To address both concerns, we maintained the environment at least ~3°C cooler than the lowest experimental temperature.

This ensures that low experimental temperatures can be maintained and also results in faster cooling to this low level. With this approach, heating and cooling occur on comparable ~minutes timescales (Figure 13D).

The thermoPlate enables rapid characterization of new thermogenetic tools, where temperature acts as an inducer for genetic or protein activity. We demonstrated this ability by systematically measuring the steady-state, kinetics, and dynamics of ELP53, an elastin-like peptide that forms condensates above a critical temperature. Although ELP phase separation is rapid, the fast heating of the thermoPlate was able to capture rapid ELP condensation and its slower approach to equilibrium, showing kinetics that are consistent with prior reports of ELP condensation in cells[82,83]. ELP condensation could also be toggled indefinitely with fast minutes-scale ON- and OFF-kinetics. Such rapid clustering matches the timescales of even the fastest optogenetic clustering approaches[92]. In a separate report, the thermoPlate was used to systematically characterize the thermogenetic Melt protein, further demonstrating the potential of the thermoPlate for thorough characterization of temperature-sensitive proteins[93].

The thermoPlate also empowers studies of native cellular responses to temperature, which we demonstrated by exploring the dynamics of the stress granule (SG) formation in response to time-varying heat-shock temperatures. We found a rich set of dynamic features of SG formation that respond to both the time and temperature of heat stress in a non-linear manner. Rather than a binary response, SG formation differed with each additional degree of heating above 41°C, with a maximal peak amplitude at 44°C. Notably, SGs showed adaptation to heat stress, such that G3BP1 puncta spontaneously dissolved despite persistent heating. Adaptation of SGs has been previously reported in the context of oxidative stress[94] and viral infection[95]. Such adaptation is consistent with negative feedback, including through transcription of heat shock proteins (HSPs)[96–100] and of suppressors of the integrated stress response including GADD34[95,101,102]. Nevertheless, to our knowledge the adaptation of SGs to chronic

heat stress has not been previously reported, demonstrating the utility of simultaneous thermal control and live-cell imaging.

Heat stress resulted in the formation of at least two types of biochemical memories. A 1hr pulse of stress was sufficient to suppress SG formation upon subsequent stress, with maximal suppression observed 3-6 hrs after the initial stress pulse. These kinetics are in line with a recent finding that 1 hr of heat stress induced suppressed activation of the integrated stress response after a second heat pulse[95]. However, this prior work did not observe the status of SG formation during this second pulse. Notably, our measurements also revealed SG suppression after only 15 and 30 min of initial heat shock. With these shorter durations, the strength of SG suppression increased with increasing temperature of prior heat shock. A second form of biochemical memory appeared in the kinetics of SG dissolution after stress removal. This memory was observed immediately after removal of heat stress but only above 44°C, consistent with fast post-translational mechanisms like protein clustering distinct from SG formation[103]. While further work will be required to identify the specific mechanisms that underlie our observations, our results highlight the discovery potential of instrumentation for easy, precise, and dynamic control of temperature under a microscope.

CONCLUSIONS AND FUTURE DIRECTIONS

Melt was able to generate multiple temperature sensitive circuits to control a large variety of post-translational modifications. Many of these may find use in future therapeutic applications. Of note, meltCasp1 was demonstrated in-vivo, granting it the most potential for therapeutic application. Manipulation of cell death could be used to locally activate cell death, activating a localized immune response, which has been shown to be an effective cancer therapeutic[104-106]. Cell death could also be used as a method of rapid release of therapeutic biologics such as nanobodies from encapsulated cell populations under the skin. Beyond therapeutics, Melt could find use in biological manufacturing, where it is often necessary to modulate the growth or production rates of living cells. Temperature control is a built in feature of most bioreactors, permitting control without the need for large amounts of expensive exogenous chemicals. Moreover, the general design principles behind Melt also could be applied to other thermogenetic proteins. ELPs show similar ability to cluster in response to temperature, perhaps allowing for similar activation of clustering based effectors such as caspases. However, ELPs would operate in a “heat on” manner, permitting activation through addition of heat rather than cold.

While Melt has shown general applicability, a detailed understanding of its underlying structure and the changes that take place with temperature are yet to be developed. Isolation of a minimal temperature sensing peptide could enable application of Melt to control protein functions beyond membrane binding and clustering. asLOV2 has similarly been adopted as a generalizable allosteric control method using light as an input based on its well understood structure[107]. Structural insight may also allow for rational tuning of Melt temperature sensing range as well as kinetics of association/dissociation, as current tuning demonstrated in this manuscript required fusion to separate peptide sequences or fortuitous identification of single point mutations.

The development of the thermoPlate enabled rapid identification of unique temperature sensitive phenotypes in synthetic thermogenetic systems such as Melt and in native temperature sensing in mammalian cell lines. The discovery of stress granule adaptation demonstrates the unique potential of high throughput, dynamic, microscopy compatible temperature control. However, future work is required to identify the underlying mechanisms of stress granule suppression. Open questions remain regarding if it is an evolved signaling network, a physical property of the molecules underlying the response, or a result of systemic damage to the cell. Future work will endeavor to characterize the processes responsible for this behavior. Understanding the dynamic properties of stress signaling may reveal unique methods of manipulating stress signaling with eventual therapeutic applications, for example, by overcoming cancer cells' resistance to stress conditions.

APPENDIX A: METHODS

Chapter 1 Methods:

Cell Culture

Lenti-X HEK 293T cells were maintained in 10% fetal bovine serum (FBS) and 1% penicillin/streptomycin (P/S) in DMEM. NIH 3T3 cells were maintained in 10% calf serum and 1% P/S in DMEM. All cells were cultured in standard cell culture incubators at 37 °C and 5% CO2. Drosophila Schneider 2 (S2) cells were maintained in Schneider's Drosophila Medium with 10% heat-inactivated Fetal Bovine Serum at room temperature. All cell lines were purchased commercially (Lenti-X HEK 293T: Takarabio 632180; NIH 3T3: ATCC CRL-1658; S2: ThermoFisher R69007). Cell lines were not verified after purchase. Cells were not cultured in proximity to commonly misidentified cell lines.

Plasmid design and assembly

Constructs for stable transduction in mammalian cells were cloned into the pHR lentiviral backbone with an SFFV promoter driving the gene of interest. The pHR backbone was linearized using MluI and NotI restriction sites. BcLOV4, iLID, BFP, SOScat, and iSH coding DNA fragments were generated via PCR and inserted into the pHR backbone via HiFi cloning mix (New England Biolabs). For expression in Drosophila S2 cells, BcLOV-mCherry, BcLOV-iSH, and BcLOV-SOScat were amplified and inserted into the pbphi-nanos promoter-αTubulin 3'UTR vector44 between the NheI and BamHI restriction sites. The resulting vectors were digested with NotI and XhoI to replace the nanos protomer with the metallothionein promoter (pMt)45, which was synthesized by gBlocks gene fragments (Integrated DNA Technologies). The pMt promoter permits inducible expression in the presence of heavy metals, e.g. copper. For zebrafish mRNA expression experiments, BcLOV-mCherry, BcLOV-SOScat and ERK-KTR-BFP (adapted from Regot et al32) were amplified with primers containing att sites for Gateway

cloning. PCR amplicons were transferred into pDONR221 plasmids and sequence verified. Gateway cloning was used to transfer each insert into pCSDest plasmids 46.

Plasmid transfection.

HEK 293Ts were transfected using the following calcium phosphate method: Per 1 mL of media of the cell culture to be transfected, 50 µL of 2x HeBS28,29 buffer, 1 µg of each DNA construct, and H2O up to 94 µL was mixed. 6 µL of 2.5mM CaCl2 was added after mixing of initial components, incubated for 1:45 minutes at room temperature, and added directly to cell culture. S2 cells were transfected with Lipofectamine 3000 reagent (ThermoFisher) following the manufacturer's protocol. Transfection mixture contained 10ng/µL of DNA, 1.5% Lipofectamine 3000 reagent, and 2% P3000 reagent, and was brought up to volume with Opti-MEM (ThermoFisher). Transfection mix was incubated for 15 min at room temperature and was then added directly to the S2 cells. 100 µL of transfection mix per 1 mL of cell culture media was used. The transfected cells were imaged 72 hr after the transfection (24 hr after promoter induction).

Lentiviral packaging and cell line generation

Lentivirus was packaged by cotransfecting the pHR transfer vector, pCMV-dR8.91, and pMD2.G (Addgene #12259) into Lenti-X HEK293T. Briefly, cells were seeded one day prior to transfection at a concentration of 350,000 cells/mL in a 6-well plate. Plasmids were transfected using the calcium phosphate method. Media was removed one day post-transfection and replaced with fresh media. Two days post-transfection, media containing virus was collected and centrifuged at 800 x g for 3 minutes. The supernatant was passed through a 0.45 µm filter. 500 µL of filtered virus solution was added to 100,000 NIH3T3 cells seeded in a 6-well plate. Cells were expanded over multiple passages, and successfully transduced cells were enriched through fluorescence activated cell sorting (BD FACS Aria II).

Zebrafish maintenance and mRNA injection

For mRNA generation, pCSDest BcLOV-SOScat, pCSDest BcLOV-mCherry and pCSDest ERK-KTR-BFP were digested with NotI. mRNA was generated using the SP6 mMessage Machine kit (Invitrogen) according to the manufacturer's specifications. 400 pg of BcLOV-SOScat or BcLOV-mCherry were injected. For the KTR construct, we injected 100 pg. For double injections, mRNAs were mixed prior to injection. Embryos were derived by natural spawning in the morning of injection and injected with the desired construct(s). Imaging was performed at 24 hours post fertilization after embedding the embryos in 1% low melting point agarose in a glass bottom dish. Animal protocols (#806819) were approved by the University of Pennsylvania Institutional Animal Care and Use Committee (IACUC). Wildtype fish of the AB strain were used for experiments at the indicated time points of development. The sex of the animals cannot be determined at the embryonic stage.

Preparation of cells for plate-based experiments

96- or 384-well plates were seeded with cells, as previously described27. Briefly, wells were coated with 50uL of MilliporeSigma™ Chemicon™ Human Plasma Fibronectin Purified Protein fibronectin solution diluted 100x in PBS and were incubated at 37 °C for 30 min. NIH 3T3 cells were seeded in 96/384-well format at a density of 3500/1000 cells/well in 100/50 µL respectively and were spun down at 100 x g for 1 minute. After 24 hr, cells were starved by performing 7 80% washes with starvation media (DMEM + 1% P/S). Experiments were performed after 3 hr of starvation.

Optogenetic stimulation

The optoPlate-96 was used for optogenetic stimulation of individual wells in microwell plates 27. A single-color optoPlate was configured with two blue LEDs for maximum dynamic range of blue light intensity. Arduino IDE (version 1.8) was used to program the Arduino Micro found on the optoPlate-96. A low-profile (9 mm tall) well-plate adapter was used for experiments where we simultaneously stimulated and modulated sample temperature. A tall adapter was used for

experiments in 384-well plates, as recommended27. Stimulation time courses were performed by assigning timepoints to individual wells. Wells corresponding to different time points were started sequentially, such that all wells could be fixed simultaneously at the end of each experiment. For live cell imaging experiments, the 488 nm laser was used to stimulate BcLOV4 membrane translocation.

Temperature-controlled optoPlate experiments.

Control of sample temperature leveraged the fact that the optoPlate generates heat when operated under conditions that draw large amounts of current27. To independently control a sample's illumination conditions and its temperature, we designated 24 LEDs as "stimulation" LEDs and repurposed the remaining 72 LEDs as "heater" LEDs. Constant illumination of the 72 heater LEDs at varying intensities permitted linear and uniform control of temperature in the 24 sample wells. Experiments were performed with the heatsink fan operating at maximum speed. To perform temperature-controlled experiments, the cell culture incubator temperature was reduced to 25 °C or 30 °C and optoPlate heating was used to increase temperature according to the relationship described in Figure 2F. Sample plates were first equilibrated to the lower incubator temperature for 2 hrs, and then were equilibrated on the optoPlate to achieve the desired increased temperature for 1.5 hrs before the illumination program began.

Immunofluorescence staining

Immediately following the completion of a stimulation protocol, 16% paraformaldehyde (PFA) was added to each well to a final concentration of 4%, and cells were incubated in PFA in the dark for 10 min. Cells were then permeabilized with 100/50 µL (for 96/384-well plates) with phosphate buffered saline (PBS) + 0.1% Triton-X for 10 min. Cells were then further permeabilized with ice cold methanol for 10 min. After permeabilization, cells were blocked with 1% BSA at room temperature for 30 min. Primary antibody was diluted in PBS + 1% BSA according to the manufacturer's recommendation for immunofluorescence (phospho-p44/42

MAPK (Erk1/2) (Thr202/Tyr204), Cell Signaling #4370, 1:400 dilution; phospho-Akt (Ser473), Cell Signaling Technologies #9271, 1:800 dilution). 96/384-well wells were incubated with 50/25 µL of antibody dilution for 2 hr at room temperature (RT). Samples were incubated at room temperature in primary antibody (for two hours, after which primary antibody was removed and samples underwent five washes in PBS + 0.1% TWEEN-20 (PBS-T). Cells were then incubated with secondary antibody (Jackson Immunoresearch Alexa Fluor® 488 AffiniPure Goat Anti-Rabbit IgG (H+L)) and DAPI (ThermoFisher, #D1306, 300 nM) in PBS-T + 0.1% BSA for 1 hour at RT. Secondary antibody was removed, samples underwent 5 washes with PBS-T. Samples were imaged in PBS-T.

Imaging

Live cell imaging. Live-cell imaging was performed using a Nikon Ti2-E microscope equipped with a Yokagawa CSU-W1 spinning disk, 405/488/561/640 nm laser lines, an sCMOS camera (Photometrics), a motorized stage, and an environmental chamber (Okolabs). HEK 293Ts expressing BcLOV-mCh were imaged with a 20X objective at variable temperatures and 5% CO2. Cells were incubated at the desired temperature for 2 hours before imaging to ensure cells equilibrated at the desired temperature. The temperature probes were submerged in PBS in wells of a 96-well plate, and the probe/plate apparatus was placed on the microscope stage inside the environmental chamber to record temperatures during imaging. BcLOV4 was stimulated using a 488nm laser. Zebrafish and Drosophila S2 cells were imaged at RT using a 40X oil immersion objective.

High content imaging. Fixed samples were imaged using a Nikon Ti2E epifluorescence microscope equipped with DAPI/FITC/Texas Red/Cy5 filter cubes, a SOLA SEII 365 LED light source, and motorized stage. High content imaging was performed using the Nikon Elements AR software. Image focus was ensured using image-based focusing in the DAPI channel.

Image processing and analysis

Immunofluorescence quantification. Images were processed using Cell Profiler47. Cells were segmented using the DAPI channel, and cytoplasm was identified using a 5 pixel ring around the nucleus. Nuclear and cytoplasmic fluorescence values were then exported and analyzed using R (https://cran.r-project.org/) and R-Studio (https://rstudio.com/). Data was processed and visualized using the dplyr48 and ggplot249 packages. For Figures 2G and andH,H, exponential decay functions of the form a * e−b*x were fit to data points in each condition in order to visualize the rate of decay in signaling. Curves were fit using the MATLAB R2020a cftool program.

Membrane recruitment. Membrane localization was quantified using the iLastik machine learning software50. Briefly, iLastik was used to identify pixels that correspond to the plasma membrane based on user annotations of images of cells that expressed iRFP-CAAX protein, which localizes to the plasma membrane. The resulting image masks were imported into Cell Profiler and were used to quantify the amount of BcLOV4 membrane localization within the same frame. Total BcLOV4, membrane-localized BcLOV4, and total iRFP-CAAX intensity was recorded and further processed in R. Bleaching was corrected by dividing the total intensity of masked mCh images by the total intensity of mCh in the original unmasked image. This method assumed that loss of fluorescence was not due to degradation, which we empirically confirmed. Zebrafish and Drosophila BcLOV4 membrane recruitment in Figure 5 was performed by manually comparing the pixel intensity of membrane and cytoplasmic intensities in ≥10 cells.

Modeling

The 3-parameter model found in Figure 3 was based on the following observations: 1) The rate of transition from the temperature inactivated (TI) to the dark state can be approximated as 0 because BcLOV4 inactivation is effectively irreversible (**Figure 2C**). 2) The rate of BcLOV4 transition from the dark state directly to the TI state can be approximated as 0 because BcLOV4 could be strongly activated even when pre-incubated for 2 hours before stimulation across a

wide range of experimental temperatures, with no obvious correlation between temperature and signal strength. 3) The rate of BcLOV4 transition from the TI state to the lit state is 0 because temperature-inactivated membrane recruitment and signal activation decay to zero, whereas a non-zero reversion to the lit state would result in a non-zero equilibrium between lit and inactivated state.

Under these assumptions, the following equations were used to model BcLOV4 activity. These equations allow only for bi-directional BcLOV4 movement between the dark and lit state and irreversible movement from the lit state to the temperature inactivated state.

$$\frac{dD}{dt} = -D * k1 + L * k2$$

(eq. 1)

$$\frac{dL}{dt} = D * k1 - L * k2 - TI * k3$$

(eq. 2)

$$\frac{dTI}{dt} = L * k3$$

(eq. 3)

D = Dark State BcLOV4

L = Lit State BcLOV4

TI = Temperature Inactivated State BcLOV4

k1 = Dark to Lit state transition rate

k2 = Lit to Dark state transition rate

k3 = Lit to Temperature Inactivated state transition rate

This system of equations was implemented in MATLAB and was solved numerically using the Euler method. The rate constants k1, k2, and k3 were found by fitting the model to live cell imaging data of BcLOV4 membrane translocation through minimization of mean squared error

(MSE)(**Figure 3F**). Fitting was performed using a custom script that iteratively calculated vertical R-squared across a coarse-grained range of parameter values, and then testing a more finely-resolved set of values centered on the best fitting value chosen from the previous iteration.

Under the assumption that:

$k1,k2 \gg k3$

(eq. 4)

k1 and k2 were found by setting k3 = 0 and fitting observed BcLOV4 translocation kinetics over short (1 minute) time periods, yielding the following rate constants:

$k1=60\pm5 min^{-1}, k2=1.5\pm0.2 min^{-1}$

k3 was then determined by keeping k1 and k2 constant and fitting k3 to observed decay rates at each temperature.

The transfer function model of SOScat-to-ppErk transmission was implemented using the image processing toolbox in MATLAB. Based on previous work26, we hypothesized that the transfer function could be modeled as a 1° or 2° low-pass filter (LPF):

$1\circ LPF: H(s)=\frac{\omega_0}{s+\omega_0}$

(eq. 5)

$2\circ LPF: H(s)=\frac{\omega_0^2}{(s+\omega_0)^2}$

(eq. 6)

where H(s) is the ratio between system input and output, s is the complex variable (frequency), and ω0 is the cutoff frequency. To discriminate between these potential models, we measured ppErk in cells when stimulated by a dynamic 2 min ON/2 min OFF pulse train of light, which corresponds to a frequency that should be ~90% suppressed by the second order LPF, but substantially less-suppressed (~40%) by a first order LPF (**Figure 4B**). We integrated the 1° or 2° LPF models into our model of BcLOV4 translocation, and we fit these integrated models to

the data as described above. We found that dynamic Erk stimulation through BcLOV4 translocation was best described by a 1° LPF with a 2 mHz cutoff frequency.

For all experiments related to modeling, illumination duty cycle was used to modulate the intensity of BcLOV4 stimulation. Duty cycle parameters were limited to patterns where the OFF period was < ~1 min to ensure that BcLOV4 membrane recruitment was maintained at intermediate levels, as determined by its measured inactivation kinetics15.

Chapter 2 Methods:

Cell Culture

Lenti-X HEK 293T cells were maintained in 10% fetal bovine serum (FBS) and 1% penicillin/streptomycin (P/S) in DMEM. (Lenti-X HEK 293T: Takarabio 632180). Cell lines were not verified after purchase. Cells were not cultured in proximity to commonly misidentified cell lines.

Plasmid design and assembly

Constructs for stable transduction and transient transfection were cloned into the pHR lentiviral backbone with a CMV promoter driving the gene of interest. Melt mutations were introduced to WT BcLOV4 (Provided by Brian Chow) (Addgene Plasmid #114595) via whole backbone PCR using primers containing the target mutation. Mutations were introduced using the same primers on BcLOV4-ITSN1 (Provided by Brian Chow) (Addgene #174509) to generate MeltITSN1-37. Melt-PB fusions were generated via whole backbone PCR using primers containing PB coding sequences (**Figure 7B**). PCR products were circularized via ligation (New England Biolabs). For Melt-effector fusions, the pHR backbone was linearized using MluI and NotI restriction sites. Melt, TEVp (Addgene Plasmid #8827), EGFR (sourced from Opto-hEGFR, which was a kind gift from Dr. Harold Janovjak), SOS [22], and Caspase-1 (Provided by Peter Broz) [46] were generated

via PCR and inserted into the pHR backbone via HiFi cloning mix (New England Biolabs). All Melt37/40-Effector fusions were generated by amplifying Melt37/40 with primers that amplified the region downstream of a.a.96 such that the final Melt variants contained a a.a.1-96 deletion. NLS/NES insertions were generated via backbone PCRs with NLS/NES sequences incorporated into the primers. To construct FlipGFP-BFP-CAAX, the two fragments of FlipGFP B1-9 and B10-E5-B11-TEVcs-K5 were amplified from Addgene Plasmid #124429 via PCR. tagBFP [22] was amplified using primers containing a CAAX membrane binding sequence. These fragments were assembled in the linearized PHR backbone via HiFi cloning mix in the order B1-9-P2A-B10-E5-B11-TEVcs-K5-tagBFP-CAAX. In order to reduce affinity of TEVp for the TEV cut site (cs) and lower basal proteolysis, the canonical cut site ENLYFQS was mutated to ENLYFQL [53] via whole backbone PCR using primers harboring the mutation. GFP-CAAX was generated via PCR of eGFP using primers containing the CAAX sequence and cloned into the linearized viral backbone using HiFi cloning mix.

Plasmid transfection.

HEK 293T cells were transfected using the calcium phosphate method, as follows: Per 1 mL of media of the cell culture to be transfected, 50 µL of 2x HeBS[28,29] buffer, 1 µg of each DNA construct, and H_2O up to 94 µL was mixed. 6 µL of 2.5mM $CaCl_2$ was added after mixing of initial components, incubated for 1:45 minutes at room temperature, and added directly to cell culture.

Lentiviral packaging and cell line generation

Lentivirus was packaged by cotransfecting the pHR transfer vector, pCMV-dR8.91 (Addgene, catalog number 12263), and pMD2.G (Addgene, catalog number 12259) into Lenti-X HEK293T. Briefly, cells were seeded one day prior to transfection at a concentration of 350,000 cells/mL in a 6-well plate. Plasmids were transfected using the calcium phosphate method. Media was

removed one day post-transfection and replaced with fresh media. Two days post-transfection, media containing virus was collected and centrifuged at 800 x g for 3 minutes. The supernatant was passed through a 0.45 µm filter. 500 µL of filtered virus solution was added to 700,000 HEK293T cells seeded in a 6-well plate. Cells were expanded over multiple passages, and successfully transduced cells were enriched through fluorescence activated cell sorting (Aria Fusion).

Preparation of cells for plate-based experiments

All experiments were carried out in Cellvis 96 well plates (#P96-1.5P). Briefly, wells were coated with 50uL of MilliporeSigma™ Chemicon™ Human Plasma Fibronectin Purified Protein fibronectin solution diluted 100x in PBS and were incubated at 37 °C for 30 min. HEK 293T cells were seeded in wells at a density of 35,000 cells/well in 100 µL and were spun down at 20 x g for 1 minute. In experiments requiring starvation (for all experiments involving SOS and EGFR constructs), after 24 hr, cells were starved by performing 7 80% washes with starvation media (DMEM + 1% P/S). Experiments were performed after 3 hr of starvation.

Fixing and Immunofluorescence staining

Immediately following the completion of a temperature stimulation protocol, 16% paraformaldehyde (PFA) was added to each well to a final concentration of 4%, and cells were incubated in PFA for 10 min. For immunofluorescence staining, cells were then permeabilized with 100 µL phosphate buffered saline (PBS) + 0.1% Triton-X for 10 min. Cells were then further permeabilized with ice cold methanol for 10 min. After permeabilization, cells were blocked with 1% BSA at room temperature for 30 min. Primary antibody was diluted in PBS + 1% BSA according to the manufacturer's recommendation for immunofluorescence (phospho-p44/42 MAPK (Erk1/2) (Thr202/Tyr204), Cell Signaling #4370, 1:400 dilution; phospho-Rb (Ser807/811)

Cell Signaling #9308, 1:800 dilution; Anti-Human G3BP1, BD Biosciences #611126, 1:500 dilution). Wells were incubated with 50 µL of antibody dilution for 2 hr at room temperature (RT), after which primary antibody was removed and samples underwent five washes in PBS + 0.1% TWEEN-20 (PBS-T). Cells were then incubated with secondary antibody (Jackson Immunoresearch Alexa Fluor® 488 AffiniPure Goat Anti-Rabbit IgG (H+L) or Invitrogen Goat anti-Mouse IgG (H+L) Cross-Adsorbed Secondary Antibody, DyLight™ 650) and DAPI (ThermoFisher, #D1306, 300 nM) in PBS-T + 0.1% BSA for 1 hour at RT. Secondary antibody was removed, samples underwent 5 washes with PBS-T. Samples were imaged in PBS-T.

Imaging

Live-cell imaging. Live-cell imaging was performed using a Nikon Ti2-E microscope equipped with a Yokagawa CSU-W1 spinning disk, 405/488/561/640 nm laser lines, an sCMOS camera (Photometrics), a motorized stage, and an environmental chamber (Okolabs). HEK 293Ts expressing the construct of interest were imaged with a 20X or 40X objective at variable temperatures and 5% CO_2. Optogenetic BcLOV4 was stimulated using a 488nm laser.

High content fixed-cell imaging. Fixed samples were imaged using a Nikon Ti2E epifluorescence microscope equipped with DAPI/FITC/Texas Red/Cy5 filter cubes, a SOLA SEII 365 LED light source, and motorized stage. High content imaging was performed using the Nikon Elements AR software. Image focus was ensured using image-based focusing in the DAPI channel.

Image processing and analysis

Immunofluorescence quantification. Images were processed using Cell Profiler. Cells were segmented using the DAPI channel, and cytoplasm was identified using a 5 pixel ring around the nucleus. Nuclear and cytoplasmic fluorescence values were then exported and analyzed

using R (https://cran.r-project.org/) and R-Studio (https://rstudio.com/). Data was processed and visualized using the tidyR [54] and ggplot2 [55] packages.

Membrane recruitment. Membrane localization was quantified using the MorphoLibJ plugin for ImageJ [56]. Briefly, MorphoLibJ was used to segment single cells based on a constitutively membrane bound GFP-CAAX marker. The resulting segmentation was imported into Cell Profiler and was used to quantify the mean mCherry (fused to the protein of interest) localized to the membrane as well as mean mCh per cell. Mean mCh and membrane-localized mCh intensity was recorded and further processed in R. Differences in expression levels were corrected for by dividing the mean membrane intensity of mCh by mean cell mCh. Membrane binding data was then normalized such that minimum membrane binding was represented as 1.0 to match the membrane binding levels of a cytoplasmic mCh.

FlipGFP Quantification. Cells expressing membrane bound FlipGFP-CAAX and the indicated TEVp construct were grown at the indicated temperature and fixed in 4% PFA after 24 hours. FlipGFP was tethered to the membrane via a Blue Fluorescent Protein (TagBFP)-CAAX fusion. BFP-CAAX remained tethered to the membrane before and after proteolysis and thus could be used as a membrane marker. This marker was used to segment single cells using the same workflow used for membrane recruitment quantification. Single cell GFP levels were quantified using Cell Profiler and used as an indicator of relative levels of proteolysis.

Nuclear Localization. To quantify nuclear localization of a protein of interest, cells expressing a GFP-CAAX membrane marker (see above) were transfected with an H2B-iRFP nuclear marker. The above workflow was used to segment individual cells based on the membrane marker. This segmentation was imported to CellProfiler, which was also used to segment nuclei based on iRFP imaging. Each nucleus was then assigned to a parent cell. Nuclei were assigned to a cell if

>90% of the nucleus object was contained by the cell object. Membrane segmented cells that contained no nuclei objects or nuclei that were not within a parent cell were eliminated from quantification. Finally, nuclear to total cell mCherry (used as a marker fused to the protein of interest) was calculated and recorded for each cell.

Annexin Staining and Quantification. Annexin V-647 (Invitrogen A23204) was added to 100 µL of cell culture at a 1:100 final dilution. A final concentration of 1 mM $CaCl_2$ was also added to each well to allow Annexin V cell labeling. Cell media was removed and replaced with Annexin V media 30 min prior to imaging. To quantify Annexin V, images of cells expressing MeltCasp1-37 or Melt-37 both with a GFP fusion were used to create GFP masks using CellProfiler's threshold function. Annexin images were masked for GFP positive pixels. The total masked Annexin image intensity was recorded and normalized by the number of GFP positive pixels (cell area per image) in each image.

Cell Area Quantification. Cell area was measured semi-manually. Images of cells expressing MeltITSN1-37 and Melt-37 were imaged and resulting images were thresholded in ImageJ such that cell positive pixels were set to 1 and background pixels were set to 0. Cells were manually chosen for quantification and regions containing the cell of interest were drawn by hand. Measuring integrated pixel intensity of these regions gave rise to the number of cell positive pixels in that region which was used as a metric of total cell area.

Curve fitting

Data points for Melt variant equilibrium membrane binding at various temperatures were fit to the Hill Equation (Eq.1). MATLAB was used to minimize the error between the sigmoid function and each data point. The characteristic function used for fitting was:

$$F(x) = A * x^B/(C^B + x^B) \text{ (Eq. 1)}$$

A, B, and C were used as the adjusted parameters. These curves are displayed in **Figure 7E, 9D, and 9H** with datapoints overlaid. The associated code can be found in this manuscript's code repository (https://rb.gy/1k7tc).

Mouse maintenance

Animal experiments were performed following Protocol 807519 approved by the UPenn Institutional Animal Care and Use Committee (IACUC). NSG mice (6–8 weeks old, male) purchased from and housed by the Perelman School of Medicine Stem Cell and Xenograft Core.

H3122 xenografts

Xenografts were performed by suspending $2x10^6$ H3122 cells expressing the indicated constructs in 100 µL of PBS+2% FBS and mixing with 100 µL of VitroGel (The Well Biosciences #VHM01). This mixture was kept in a 37°C water path while mice were prepared for injection. Mice were anesthetized using 2.5% isoflurane and 200 µL of the cell suspension was injected subcutaneously on each mouse flank. Mice were maintained under a heat lamp during injection and while recovering from anesthesia.

Thermoelectric cooling device

The thermoelectric cooling device consists of two Peltier plates connected in series. The smaller Peltier plate (Digikey 102-4428-ND) is attached by its heating face to the cooling face of the larger Peltier plate (CNBTR TES1-4902) using thermally conductive tape (AI AIKENUO 8541602030). An electronic thermometer (Walfront MF55) is attached the cooling face of the smaller Peltier and covered with a soft thermal pad (Arctic Cooling ACTPD00004A). The thermal pad provides a soft surface when pressed against the mouse's skin. An aluminum heat sink (Jienk JT371-374) is attached to the heating face of the larger Peltier plate to dissipate

excess heat. Finally, a fan (Winsinn FAN40105V) is attached on top of the heat sink for additional heat dissipation. An Arduino microcontroller (Arduino A000053) obtains readings from the electronic thermometer and adjusts the on/off state of a transistor (Bridgold B07R49F39B) that regulates power delivery to the Peltier assembly. 3.5V is supplied to the Peltier plates when cooling is desired. The fan is constantly turned on even when no cooling is needed.

Local cooling of mouse xenografts

Mice were anesthetized using 2.5% isoflurane, placed on a heating pad (37°C), and kept under anesthesia using a nose cone, with isoflurane percentage adjusted to maintain at least 10 breaths per 15 seconds. Local cooling was applied to the designated flank by pressing the thermoelectric cooling device to the skin with enough pressure to slightly depress the surrounding tissue.

Luminescence imaging

Mice were injected with 200 µL of 15 mg/mL D-Luciferin (GoldBio LUCK) via intraperitoneal injection 10 minutes prior to imaging. Mice were then anesthetized with 2.5% isoflurane and luminescence was recorded using an IVIS Spectrum imaging system every ~5 minutes until the luminescent signal was maximal. Mice were then allowed to recover from anesthesia under a heat lamp.

Chapter 3 Methods:

PID Implementation

PID (Proportional, Integral, Derivative) control was implemented using a discrete form of the standard PID algorithm. PID constants were generated empirically by testing several combinations. In brief, the Arduino collects the temperature of every well every ~2 seconds. These values are used to calculate the current error (proportional), change in error from the

previous reading per unit time (derivative), and integral (time weighted sum of all past error). The algorithm applies the PID constants to each error value and calculates a new duty ratio to apply to the corresponding heater. For more detailed information on programming architecture, see the **Code** section of the **Repository**.

thermoPlate Calibration

Calibration was performed by placing a thermoPlate on a 96 well plate containing PBS. This assembly was equilibrated in a standard mammalian cell culture incubator at ~25°C. Two digital thermometers (RC-4 Elitech Digital Temperature Data Logger) were placed inside two 15mL conical tubes filled with water and sealed with parafilm (to prevent evaporation). Both conical tube/thermometer were placed next to the thermoPlate, and a plastic box was placed over the thermoPlate and thermometers to avoid variation due to airflow. The average of the two digital thermometers was recorded as the true temperature. 5 temperature readings were recorded from each well. The average of those 5 readings was assigned as the final temperature reading of that well. The incubator temperature was then increased to 30°C and allowed to equilibrate for 2 hours. Readings from the thermoPlate and the digital thermometers were recorded, and this procedure was repeated in 5°C steps until 45°C. For each well, the temperature readings of the thermoPlate vs digital thermometers was then plotted, and the slope and y-intercept of the linear fit were extracted. These values were used to calibrate each raw temperature reading during thermoPlate operation.

thermoPlate Modeling

A model of heat transfer within a thermoPlate-heated 96-well plate was made in MATLAB to simulate the temperature of each well given a desired heating input. Well temperatures were simulated through time. At each timestep, the instantaneous heat derivative of each well was calculated and multiplied by the simulation timestep to obtain the well's temperature at the next

timestep. The model uses 8 parameters. $\mathbf{H_p}$ describes heat transfer between neighboring unheated wells. Around heated wells, $\mathbf{H_{left}}$, $\mathbf{H_{right}}$, $\mathbf{H_{top}}$, and $\mathbf{H_{bottom}}$ describe heat transfer between the heated well and its neighbors to the left, right, top, and bottom, respectively. This was done to capture the consistent asymmetries seen in temperature around wells that are actively heated. $\mathbf{H_e}$ describes heat transfer from an edge well to the environment, ***loss*** describes a consistent loss of heat from each well to the environment. Finally, ***heat*** is a constant temperature increment that is added to each heated well during a simulation step where the well is below its set temperature. When a heated well is at or above its setpoint, this ***heat*** is not added for that step. Parameters were obtained by fitting the model to eight real datasets and averaging resultant 8 parameter sets to obtain generalizable parameters. Fitting was done by minimizing an error function, defined as the difference between the simulation and the real data summed across every well and timepoint. Minimization was done using the MATLAB function fminsearch.

Cell Culture

HeLa cells were maintained in 10% fetal bovine serum (FBS) and 1% penicillin/streptomycin (P/S) in DMEM. Cell lines were not verified after purchase. Cells were not cultured in proximity to commonly misidentified cell lines.

Plasmid design and assembly

Constructs for stable transduction and transient transfection were cloned into the pHR lentiviral backbone with an SFFV promoter driving the gene of interest. The pHR backbone was linearized using MluI and NotI restriction sites. G3BP1 (Ophir Shalem Lab) and mCherry inserts were generated via PCR and cloned into the linearized viral backbone as a single fusion protein using HiFi cloning mix (NEB). H2B-iRFP nuclear marker was (Addgene Plasmid #90237). ELP_{48} was obtained from Addgene (Addgene Plasmid #68395). Sequencing of ELP_{48} showed it

contained 44 ELP repeats. ELP_{48} was digested using NdeI and BamHI and ligated into a small backbone pTA for the ease of cloning. ELP_9 was ordered as primers and inserted via HiFi into the pTA-ELP_{48} linearized with AgeI and BsmBI, generating pTA-ELP_{53}. EGFP was then amplified and inserted via HiFi to pTA-ELP_{53}, which was linearized using MluI and XcmI. ELP_{53}-EGFP was then subcloned via HiFi to the viral backbone pHR digested with MluI and NotI.

Plasmid transfection.

HEK 293T cells were transfected using the calcium phosphate method, as follows: Per 1 mL of media of the cell culture to be transfected, 50 µL of 2x HeBS buffer, 1 µg of each DNA construct, and H_2O up to 94 µL was mixed. 6 µL of 2.5mM $CaCl_2$ was added after mixing of initial components, incubated for 1:45 minutes at room temperature, and added directly to cell culture.

Lentiviral packaging and cell line generation

Lentivirus was packaged by cotransfecting the pHR transfer vector, pCMV-dR8.91 (Addgene, catalog number 12263), and pMD2.G (Addgene, catalog number 12259) into Lenti-X HEK293T. Briefly, cells were seeded one day prior to transfection at a concentration of 350,000 cells/mL in a 6-well plate. Plasmids were transfected using the calcium phosphate method. Media was removed one day post-transfection and replaced with fresh media. Two days post-transfection, media containing virus was collected and centrifuged at 800 x g for 3 minutes. The supernatant was passed through a 0.45 µm filter. 500 µL of filtered virus solution was added to 700,000 HeLa cells seeded in a 6-well plate. Cells were expanded over multiple passages, and successfully transduced cells were enriched through fluorescence activated cell sorting (BD FACS Aria Fusion).

Preparation of cells for plate-based experiments

All experiments were carried out in Falcon™ 353219 Black 96 well plates. Briefly, wells were coated with 50 uL of MilliporeSigma™ Chemicon™ Human Plasma Fibronectin Purified Protein fibronectin solution diluted 100x in PBS and were incubated at 37 °C for 30 min. HeLa or HEK 293T cells were seeded in wells at a density of 60,000 cells/well in 100 µL and were spun down at 20 x g for 1 minute to ensure an even distribution of cells across the wells. For imaging ELPs, HEK 293T cells were transfected with GFP-ELP_{53} and H2B-iRFP 12-24 hours post-seeding in 96 well plates using the calcium phosphate method. Transfection mix/media was removed 24 hours post transfection and replaced with fresh media. Cells were imaged within 4-8 hours of this media change.

Imaging

Live-cell imaging. Live-cell imaging was performed using a Nikon Ti2-E microscope equipped with a Yokagawa CSU-W1 spinning disk, 405/488/561/640 nm laser lines, an sCMOS camera (Photometrics), a motorized stage, and an environmental chamber (Okolabs). Cells expressing the construct of interest were imaged with a 20X air objective at variable temperatures and 5% CO_2.

Imaging quantification. Images were processed using Cell Profiler [33]. Cells were segmented using the H2B-iRFP imaging channel, and cytoplasm was identified using a 20 pixel ring around the nucleus. Nuclear and cytoplasmic fluorescence values were then exported and analyzed using R (https://cran.r-project.org/) and R-Studio (https://rstudio.com/). Data was processed and visualized using the tidyR [46] and ggplot2 [47] packages. Stress granules and ELP condensates were quantified by averaging the maximum pixel intensity of each cell within a frame and then averaging those values across multiple replicates.

BIBLIOGRAPHY

1. CAR T Cells: Engineering Immune Cells to Treat Cancer. https://www.cancer.gov/about-cancer/treatment/research/car-t-cells (2013).
2. Palacios, A. M., Korus, P., Wilkens, B. G. C., Heshmatpour, N. & Patnaik, S. R. Revolutionizing in vivo therapy with CRISPR/Cas genome editing: breakthroughs, opportunities and challenges. *Frontiers in Genome Editing* **6**, (2024).
3. Paunovska, K., Loughrey, D. & Dahlman, J. E. Drug delivery systems for RNA therapeutics. *Nat. Rev. Genet.* **23**, 265–280 (2022).
4. Synthetic therapeutic gene circuits in mammalian cells. *FEBS Lett.* **588**, 2537–2544 (2014).
5. Sterner, R. C. & Sterner, R. M. CAR-T cell therapy: current limitations and potential strategies. *Blood Cancer J.* **11**, 1–11 (2021).
6. Benefits and Risks. *NHLBI, NIH* https://www.nhlbi.nih.gov/health/genetic-therapies/benefits-risks.
7. Grünberg, R. & Serrano, L. Strategies for protein synthetic biology. *Nucleic Acids Res.* **38**, 2663 (2010).
8. Edwards, S. R. & Wandless, T. J. The Rapamycin-Binding Domain of the Protein Kinase mTOR is a Destabilizing Domain. *J. Biol. Chem.* **282**, 13395 (2007).
9. Wu, J. *et al.* Modulating gene regulation function by chemically controlled transcription factor clustering. *Nat. Commun.* **13**, 1–15 (2022).
10. Guntas, G. *et al.* Engineering an improved light-induced dimer (iLID) for controlling the localization and activity of signaling proteins. *Proc. Natl. Acad. Sci. U. S. A.* **112**, 112–117 (2015).
11. Kennedy, M. J. *et al.* Rapid blue-light-mediated induction of protein interactions in living cells. *Nat. Methods* **7**, 973–975 (2010).

12. Shimizu-Sato, S., Huq, E., Tepperman, J. M. & Quail, P. H. A light-switchable gene promoter system. *Nat. Biotechnol.* **20**, 1041–1044 (2002).
13. Hang, H. C., Pratt, M. R. & Prescher, J. A. *Advanced Chemical Biology: Chemical Dissection and Reprogramming of Biological Systems*. (John Wiley & Sons, 2023).
14. Kawano, F., Suzuki, H., Furuya, A. & Sato, M. Engineered pairs of distinct photoswitches for optogenetic control of cellular proteins. *Nat. Commun.* **6**, 6256 (2015).
15. Zhou, X. X., Chung, H. K., Lam, A. J. & Lin, M. Z. Optical control of protein activity by fluorescent protein domains. *Science* **338**, 810–814 (2012).
16. Wu, Y. I. *et al.* A genetically encoded photoactivatable Rac controls the motility of living cells. *Nature* **461**, 104–108 (2009).
17. Bugaj, L. J., Choksi, A. T., Mesuda, C. K., Kane, R. S. & Schaffer, D. V. Optogenetic protein clustering and signaling activation in mammalian cells. *Nat. Methods* **10**, 249–252 (2013).
18. Boyden, E. S., Zhang, F., Bamberg, E., Nagel, G. & Deisseroth, K. Millisecond-timescale, genetically targeted optical control of neural activity. *Nat. Neurosci.* **8**, 1263–1268 (2005).
19. Glantz, S. T. *et al.* Directly light-regulated binding of RGS-LOV photoreceptors to anionic membrane phospholipids. *Proc. Natl. Acad. Sci. U. S. A.* **115**, E7720–E7727 (2018).
20. He, L. *et al.* Optical control of membrane tethering and interorganellar communication at nanoscales. *Chem. Sci.* **8**, 5275–5281 (2017).
21. Piraner, D. I. *et al.* Going Deeper: Biomolecular Tools for Acoustic and Magnetic Imaging and Control of Cellular Function. *Biochemistry* **56**, 5202–5209 (2017).
22. Miller, I. C. *et al.* Enhanced intratumoural activity of CAR T cells engineered to produce immunomodulators under photothermal control. *Nature Biomedical Engineering* **5**, 1348–1359 (2021).
23. Ermakova, Y. G. *et al.* Thermogenetic control of Ca2+ levels in cells and tissues. *bioRxiv*

2023.03.22.533774 (2023) doi:10.1101/2023.03.22.533774.

24. Corbett, D. C. *et al.* Thermofluidic heat exchangers for actuation of transcription in artificial tissues. *Sci Adv* **6**, (2020).
25. Haar, G. T. & Coussios, C. High intensity focused ultrasound: physical principles and devices. *Int. J. Hyperthermia* **23**, 89–104 (2007).
26. Abedi, M. H., Lee, J., Piraner, D. I. & Shapiro, M. G. Thermal Control of Engineered T-cells. *ACS Synth. Biol.* (2020) doi:10.1021/acssynbio.0c00238.
27. Wu, Y. *et al.* Control of the activity of CAR-T cells within tumours via focused ultrasound. *Nat Biomed Eng* **5**, 1336–1347 (2021).
28. Morimoto, R. I. Cells in Stress: Transcriptional Activation of Heat Shock Genes. *Science* (1993) doi:10.1126/science.8451637.
29. Feder, M. E. & Hofmann, G. E. Heat-shock proteins, molecular chaperones, and the stress response: evolutionary and ecological physiology. *Annu. Rev. Physiol.* **61**, (1999).
30. Akerfelt, M., Morimoto, R. I. & Sistonen, L. Heat shock factors: integrators of cell stress, development and lifespan. *Nat. Rev. Mol. Cell Biol.* **11**, 545–555 (2010).
31. Biochemical Genetics of Neurospora. in *Advances in Genetics* vol. 3 33–71 (Academic Press, 1950).
32. Talavera, A. & Basilico, C. Temperature sensitive mutants of BHK cells affected in cell cycle progression. *J. Cell. Physiol.* **92**, 425–436 (1977).
33. Varadarajan, R., Nagarajaram, H. A. & Ramakrishnan, C. A procedure for the prediction of temperature-sensitive mutants of a globular protein based solely on the amino acid sequence. *Proc. Natl. Acad. Sci. U. S. A.* **93**, 13908 (1996).
34. Hurme, R., Berndt, K. D., Normark, S. J. & Rhen, M. A proteinaceous gene regulatory thermometer in Salmonella. *Cell* **90**, 55–64 (1997).
35. Piraner, D. I., Wu, Y. & Shapiro, M. G. Modular Thermal Control of Protein Dimerization.

ACS Synth. Biol. **8**, 2256–2262 (2019).

36. Christie, J. M., Salomon, M., Nozue, K., Wada, M. & Briggs, W. R. LOV (light, oxygen, or voltage) domains of the blue-light photoreceptor phototropin (nph1): binding sites for the chromophore flavin mononucleotide. *Proc. Natl. Acad. Sci. U. S. A.* **96**, 8779–8783 (1999).
37. Schwerdtfeger, C. & Linden, H. VIVID is a flavoprotein and serves as a fungal blue light photoreceptor for photoadaptation. *EMBO J.* **22**, 4846–4855 (2003).
38. McCubrey, J. A. *et al.* Roles of the Raf/MEK/ERK pathway in cell growth, malignant transformation and drug resistance. *Biochim. Biophys. Acta* **1773**, 1263–1284 (2007).
39. Chang, F. *et al.* Signal transduction mediated by the Ras/Raf/MEK/ERK pathway from cytokine receptors to transcription factors: potential targeting for therapeutic intervention. *Leukemia* **17**, 1263–1293 (2003).
40. Vanhaesebroeck, B., Stephens, L. & Hawkins, P. PI3K signalling: the path to discovery and understanding. *Nat. Rev. Mol. Cell Biol.* **13**, 195–203 (2012).
41. Yang, J. *et al.* Targeting PI3K in cancer: mechanisms and advances in clinical trials. *Mol. Cancer* **18**, 26 (2019).
42. Bugaj, L. J. *et al.* Cancer mutations and targeted drugs can disrupt dynamic signal encoding by the Ras-Erk pathway. *Science* **361**, (2018).
43. Hino, N. *et al.* ERK-Mediated Mechanochemical Waves Direct Collective Cell Polarization. *Dev. Cell* **53**, 646–660.e8 (2020).
44. Johnson, H. E. *et al.* The Spatiotemporal Limits of Developmental Erk Signaling. *Dev. Cell* **40**, 185–192 (2017).
45. Johnson, H. E. & Toettcher, J. E. Signaling Dynamics Control Cell Fate in the Early Drosophila Embryo. *Dev. Cell* **48**, 361–370.e3 (2019).
46. Toettcher, J. E., Gong, D., Lim, W. A. & Weiner, O. D. Light-based feedback for controlling intracellular signaling dynamics. *Nat. Methods* **8**, 837–839 (2011).

47. Toettcher, J. E., Weiner, O. D. & Lim, W. A. Using optogenetics to interrogate the dynamic control of signal transmission by the Ras/Erk module. *Cell* **155**, 1422–1434 (2013).
48. Bugaj, L. J. & Lim, W. A. High-throughput multicolor optogenetics in microwell plates. *Nat. Protoc.* **14**, 2205–2228 (2019).
49. Berlew, E. E., Kuznetsov, I. A., Yamada, K., Bugaj, L. J. & Chow, B. Y. Optogenetic Rac1 engineered from membrane lipid-binding RGS-LOV for inducible lamellipodia formation. *Photochem. Photobiol. Sci.* **19**, 353–361 (2020).
50. Berlew, E. E. *et al.* Single-Component Optogenetic Tools for Inducible RhoA GTPase Signaling. *Adv Biol (Weinh)* **5**, e2100810 (2021).
51. Hannanta-Anan, P., Glantz, S. T. & Chow, B. Y. Optically inducible membrane recruitment and signaling systems. *Curr. Opin. Struct. Biol.* **57**, 84–92 (2019).
52. Suh, B.-C., Inoue, T., Meyer, T. & Hille, B. Rapid chemically induced changes of PtdIns(4,5)P2 gate KCNQ ion channels. *Science* **314**, 1454–1457 (2006).
53. Mayr, V., Sturtzel, C., Stadler, M., Grissenberger, S. & Distel, M. Fast Dynamic Monitoring of Erk Activity at Single Cell Resolution in DREKA Zebrafish. *Front Cell Dev Biol* **6**, 111 (2018).
54. Dietler, J. *et al.* A Light-Oxygen-Voltage Receptor Integrates Light and Temperature. *J. Mol. Biol.* **433**, 167107 (2021).
55. Golic, A. E. *et al.* BlsA Is a Low to Moderate Temperature Blue Light Photoreceptor in the Human Pathogen. *Front. Microbiol.* **10**, 1925 (2019).
56. Nakasone, Y., Ono, T.-A., Ishii, A., Masuda, S. & Terazima, M. Temperature-sensitive reaction of a photosensor protein YcgF: possibility of a role of temperature sensor. *Biochemistry* **49**, 2288–2296 (2010).
57. Nakasone, Y. *et al.* Stability of dimer and domain-domain interaction of Arabidopsis phototropin 1 LOV2. *J. Mol. Biol.* **383**, 904–913 (2008).

58. Benedetti, L. *et al.* Optimized Vivid-derived Magnets photodimerizers for subcellular optogenetics in mammalian cells. *Elife* **9**, (2020).
59. Ntziachristos, V. Going deeper than microscopy: the optical imaging frontier in biology. *Nat. Methods* **7**, 603–614 (2010).
60. Ash, C., Dubec, M., Donne, K. & Bashford, T. Effect of wavelength and beam width on penetration in light-tissue interaction using computational methods. *Lasers Med. Sci.* **32**, 1909–1918 (2017).
61. Benman, W. *et al.* Temperature-responsive optogenetic probes of cell signaling. *Nat. Chem. Biol.* **18**, 152–160 (2022).
62. Pal, A. A. *et al.* Optogenetic clustering and membrane translocation of the BcLOV4 photoreceptor. *Proc. Natl. Acad. Sci. U. S. A.* **120**, e2221615120 (2023).
63. Harper, S. M., Neil, L. C. & Gardner, K. H. Structural basis of a phototropin light switch. *Science* **301**, 1541–1544 (2003).
64. Grecco, H. E., Schmick, M. & Bastiaens, P. I. Signaling from the living plasma membrane. *Cell* **144**, (2011).
65. Citri, A. & Yarden, Y. EGF–ERBB signalling: towards the systems level. *Nat. Rev. Mol. Cell Biol.* **7**, 505–516 (2006).
66. Liang, S. I. *et al.* Phosphorylated EGFR Dimers Are Not Sufficient to Activate Ras. *Cell Rep.* **22**, 2593–2600 (2018).
67. Chung, H. K. *et al.* A compact synthetic pathway rewires cancer signaling to therapeutic effector release. *Science* **364**, (2019).
68. Gao, X. J., Chong, L. S., Kim, M. S. & Elowitz, M. B. Programmable protein circuits in living cells. *Science* (2018) doi:10.1126/science.aat5062.
69. Sanchez, M. I. & Ting, A. Y. Publisher Correction: Directed evolution improves the catalytic efficiency of TEV protease. *Nat. Methods* **17**, 242 (2020).

70. Collas, P. & Aleström, P. Nuclear localization signal of SV40 T antigen directs import of plasmid DNA into sea urchin male pronuclei in vitro. *Mol. Reprod. Dev.* **45**, 431–438 (1996).
71. Dorfman, J. & Macara, I. G. STRADalpha regulates LKB1 localization by blocking access to importin-alpha, and by association with Crm1 and exportin-7. *Mol. Biol. Cell* **19**, 1614–1626 (2008).
72. Heo, W. D. *et al.* PI(3,4,5)P3 and PI(4,5)P2 lipids target proteins with polybasic clusters to the plasma membrane. *Science* **314**, (2006).
73. Regot, S., Hughey, J. J., Bajar, B. T., Carrasco, S. & Covert, M. W. High-sensitivity measurements of multiple kinase activities in live single cells. *Cell* **157**, 1724–1734 (2014).
74. Levskaya, A., Weiner, O. D., Lim, W. A. & Voigt, C. A. Spatiotemporal control of cell signalling using a light-switchable protein interaction. *Nature* **461**, 997–1001 (2009).
75. Berlew, E. E. *et al.* Designing Single-Component Optogenetic Membrane Recruitment Systems: The Rho-Family GTPase Signaling Toolbox. *ACS Synth. Biol.* **11**, 515–521 (2022).
76. Nobes, C. D. & Hall, A. Rho, rac, and cdc42 GTPases regulate the assembly of multimolecular focal complexes associated with actin stress fibers, lamellipodia, and filopodia. *Cell* **81**, 53–62 (1995).
77. Shkarina, K. *et al.* Optogenetic activators of apoptosis, necroptosis, and pyroptosis. *J. Cell Biol.* **221**, (2022).
78. Qiao, J., Peng, H. & Dong, B. Development and Application of an Optogenetic Manipulation System to Suppress Actomyosin Activity in Ciona Epidermis. *Int. J. Mol. Sci.* **24**, (2023).
79. Mackowiak, P. A. & Boulant, J. A. Fever's glass ceiling. *Clin. Infect. Dis.* **22**, (1996).
80. Halloran, M. C. *et al.* Laser-induced gene expression in specific cells of transgenic zebrafish. *Development* **127**, 1953–1960 (2000).
81. Chu, K. F. & Dupuy, D. E. Thermal ablation of tumours: biological mechanisms and

advances in therapy. *Nat. Rev. Cancer* **14**, 199–208 (2014).

82. Pastuszka, M. K. *et al.* A tunable and reversible platform for the intracellular formation of genetically engineered protein microdomains. *Biomacromolecules* **13**, 3439–3444 (2012).
83. Li, Z., Tyrpak, D. R., Park, M., Okamoto, C. T. & MacKay, J. A. A new temperature-dependent strategy to modulate the epidermal growth factor receptor. *Biomaterials* **183**, 319–330 (2018).
84. Vu, C. Q., Fukushima, S.-I., Wazawa, T. & Nagai, T. A highly-sensitive genetically encoded temperature indicator exploiting a temperature-responsive elastin-like polypeptide. *Sci. Rep.* **11**, 16519 (2021).
85. Protter, D. S. W. & Parker, R. Principles and Properties of Stress Granules. *Trends Cell Biol.* **26**, 668–679 (2016).
86. Khong, A. *et al.* The Stress Granule Transcriptome Reveals Principles of mRNA Accumulation in Stress Granules. *Mol. Cell* **68**, 808–820.e5 (2017).
87. Jain, S. *et al.* ATPase-Modulated Stress Granules Contain a Diverse Proteome and Substructure. *Cell* **164**, 487–498 (2016).
88. Nunes, C. *et al.* MSGP: the first database of the protein components of the mammalian stress granules. *Database* **2019**, (2019).
89. Markmiller, S. *et al.* Context-Dependent and Disease-Specific Diversity in Protein Interactions within Stress Granules. *Cell* **172**, 590–604.e13 (2018).
90. Youn, J.-Y. *et al.* High-Density Proximity Mapping Reveals the Subcellular Organization of mRNA-Associated Granules and Bodies. *Mol. Cell* **69**, 517–532.e11 (2018).
91. Qin, W. *et al.* Dynamic mapping of proteome trafficking within and between living cells by TransitID. *Cell* **186**, 3307–3324.e30 (2023).
92. Huang Dennis, Z., Benman, W., Dong, L. & Bugaj, L. J. Rapid Optogenetic Clustering in the Cytoplasm with BcLOVclust. *J. Mol. Biol.* **436**, 168452 (2024).

93. Benman, W. *et al.* A temperature-inducible protein module for control of mammalian cell fate. *bioRxiv* (2024) doi:10.1101/2024.02.19.581019.
94. McGurk, L. *et al.* Poly(ADP-Ribose) Prevents Pathological Phase Separation of TDP-43 by Promoting Liquid Demixing and Stress Granule Localization. *Mol. Cell* **71**, 703–717.e9 (2018).
95. Klein, P. *et al.* Temporal control of the integrated stress response by a stochastic molecular switch. *Sci Adv* **8**, eabk2022 (2022).
96. Solís, E. J. *et al.* Defining the Essential Function of Yeast Hsf1 Reveals a Compact Transcriptional Program for Maintaining Eukaryotic Proteostasis. *Mol. Cell* **69**, 534 (2018).
97. Yoo, H., Bard, J. A. M., Pilipenko, E. V. & Drummond, D. A. Chaperones directly and efficiently disperse stress-triggered biomolecular condensates. *Mol. Cell* **82**, 741–755.e11 (2022).
98. McMillan, D. R., Xiao, X., Shao, L., Graves, K. & Benjamin, I. J. Targeted disruption of heat shock transcription factor 1 abolishes thermotolerance and protection against heat-inducible apoptosis. *J. Biol. Chem.* **273**, 7523–7528 (1998).
99. Pirkkala, L., Alastalo, T. P., Zuo, X., Benjamin, I. J. & Sistonen, L. Disruption of heat shock factor 1 reveals an essential role in the ubiquitin proteolytic pathway. *Mol. Cell. Biol.* **20**, 2670–2675 (2000).
100. Krakowiak, J. *et al.* Hsf1 and Hsp70 constitute a two-component feedback loop that regulates the yeast heat shock response. *Elife* **7**, (2018).
101. Batjargal, T. *et al.* Optogenetic control of the integrated stress response reveals proportional encoding and the stress memory landscape. *Cell Syst* **14**, 551–562.e5 (2023).
102. Kojima, E. *et al.* The function of GADD34 is a recovery from a shutoff of protein synthesis induced by ER stress: elucidation by GADD34-deficient mice. *FASEB J.* **17**, 1573–1575 (2003).

103. Riback, J. A. *et al.* Stress-Triggered Phase Separation Is an Adaptive, Evolutionarily Tuned Response. *Cell* **168**, 1028–1040.e19 (2017).

104. Yatim, N. et al. RIPK1 and NF-κB signaling in dying cells determines cross-priming of CD8+ T cells. Science 350, 328–334 (2015).

105. Snyder, A. G. et al. Intratumoral activation of the necroptotic pathway components RIPK1 and RIPK3 potentiates antitumor immunity. Sci Immunol 4, (2019).

106. Zhang, Z. et al. Gasdermin E suppresses tumour growth by activating anti-tumour immunity. Nature 579, 415–420 (2020).

107. Shannon M. Harper et al. Structural Basis of a Phototropin Light Switch. Science301,1541-1544 (2003).